

---

# Magneto-transport studies in WTe<sub>2</sub>/Cr<sub>2</sub>Ge<sub>2</sub>Te<sub>6</sub> bilayers

---

Mireia Torres Sala

Supervised by: Juan F. Sierra & Sergio O. Valenzuela

Catalan Institute of Nanoscience and Nanotechnology (ICN2), BIST and CSIC, Campus UAB, Bellaterra, Barcelona, 08193, Spain.

July 2024

The recent discovery of two-dimensional (2D) ferromagnetic insulators and the continuous advancements in the fabrication of van der Waals heterostructures have enabled studying proximity-induced magnetic exchange interactions. Stacking a vdW magnetic insulator like Cr<sub>2</sub>Ge<sub>2</sub>Te<sub>6</sub> (CGT) with a 2D semimetal with strong spin-orbit coupling (SOC) like WTe<sub>2</sub> could potentially allow us to imprint magnetism in the latter, a physical property absent in its pristine form. This thesis presents a detailed investigation of magnetic proximity effects through magneto-transport studies in hybrid WTe<sub>2</sub>/CGT hetero-bilayers. This material combination could represent a building block towards realizing the quantum anomalous Hall effect, which requires the co-integration of a topological insulator, like monolayer WTe<sub>2</sub>, with a perpendicularly magnetized 2D ferromagnet such as CGT. Six devices were fabricated and electrically characterized. We observe that the annealing of the heterostructure after preparing the bilayer is a crucial step for improving the quality of the vdW interface between WTe<sub>2</sub> and CGT. Additionally, an increase in the Curie temperature of CGT, likely driven by spin-orbit coupling interfacial effects, has been observed. Notably, four out of the six annealed samples exhibited magnetic hysteretic behaviour in the transversal voltage  $V_{xy}$ . The angle dependence of the magnetoresistance in one sample was analysed to investigate whether the hysteric behaviour in  $V_{xy}$  arises from proximity-induced anomalous Hall or spin Hall magnetoresistance effect, using the spin texture in the low-symmetry WTe<sub>2</sub>.

**Keywords:** van der Waals heterostructures, proximity effects, anomalous Hall effect

---

Mireia Torres Sala: [mireia.torres@icn2.cat](mailto:mireia.torres@icn2.cat)

---

## Acknowledgements

I would like to express my gratitude for the support and guidance of my supervisor, Juan, for imparting both theoretical and experimental knowledge that enabled me to work in the laboratory efficiently. The trust he placed in me, and his constant presence have been invaluable. I am also deeply grateful to Franz for his daily help, his patience, and his willingness to explain complex concepts in multiple ways until I understood them. Being able to rely on his help at any time has been a great support.

Additionally, I would like to thank my other supervisor, Sergio, for the opportunity he provided me, and for sharing his knowledge. His clarity in addressing and resolving many of the questions that arose has been instrumental in guiding the direction of this work.

Finally, I would like to thank the entire PEN Group team—Patricia, Nandan, Carmen, Thomas, Enzo, Motomi, Joseph, Flavius, and Guillermo—for all their support and the excellent camaraderie. The mutual assistance among each other has been immensely helpful.

---

## Contents

<b>1</b>	<b>Introduction</b>	<b>1</b>
<b>2</b>	<b>Theoretical background</b>	<b>2</b>
2.1	Van der Waals materials	2
2.2	Van der Waals heterostructures	2
2.3	Proximity effects	2
2.4	Hall effect and anomalous Hall effect	3
2.4.1	Quantum anomalous Hall effect in magnetic topological insulators	4
2.5	Spin Hall magnetoresistance	5
2.6	Differentiating magnetic proximity effect and spin Hall magnetoresistance	6
<b>3</b>	<b>Experimental background</b>	<b>8</b>
3.1	Materials utilized for heterostructure fabrication	8
3.1.1	Hexagonal boron nitride	8
3.1.2	The van der Waals magnet $\text{Cr}_2\text{Ge}_2\text{Te}_6$	9
3.1.3	Tungsten ditelluride	9
3.2	Device fabrication	10
3.2.1	Pre-patterned contacts defined by electron beam lithography	10
3.2.2	Mechanical exfoliation of the source materials	10
3.2.3	Heterostructure stacking and deterministic transfer	11
3.2.4	High vacuum annealing	11
3.3	Magneto-transport measurement set-up	12
<b>4</b>	<b>Results and discussion</b>	<b>12</b>
4.1	Device overview and proximity phenomena analysis	12
4.2	Effect of annealing on device resistances	13
4.3	Magneto-transport measurements	14
4.4	In-plane magnetic field angular dependence	16
4.4.1	First axis	16
4.4.2	Second axis	18
<b>5</b>	<b>Conclusions and outlook</b>	<b>19</b>
	<b>Bibliography</b>	<b>20</b>
<b>A</b>	<b>Differentiating magnetic proximity effect and spin Hall magnetoresistance effect in a low-symmetry crystal</b>	<b>25</b>
<b>B</b>	<b>Gate dependence</b>	<b>26</b>
<b>C</b>	<b>Further details on the device overview</b>	<b>28</b>
<b>D</b>	<b>Complementary temperature dependence of the longitudinal resistance</b>	<b>29</b>
<b>E</b>	<b>Complementary magneto-transport measurements</b>	<b>30</b>
<b>F</b>	<b>Complementary angle dependence for the in-plane magnetic field</b>	<b>31</b>

---

# 1 Introduction

In recent years, there has been a significant rise in interest in the growth and isolation of atomically thin materials through different physical growth methods and from bulk van der Waals (vdW) materials. These atomically thin layers can be stacked on top of one another, forming artificial heterostructures. vdW heterostructures have emerged as a novel class of materials with unique and tunable physical properties, garnering considerable attention for their potential to exhibit a wide range of electronic, magnetic, and optical phenomenon. One such phenomenon is proximity-induced effects, where the physical properties of one layer can be imprinted onto an adjacent one through interfacial interactions. This is particularly appealing because the atomically thin nature of the constituents materials allows for efficient imprinting of short range interactions, such as spin-orbit-coupling (SOC) and magnetism. The primary goal of this research is to investigate magnetic proximity effects in vdW heterostructures, specifically focusing on bilayer systems composed of the Weyl semimetal tungsten ditelluride ( $\text{WTe}_2$ ), and chromium germanium telluride ( $\text{Cr}_2\text{Ge}_2\text{Te}_6$ , CGT), a vdW ferromagnetic insulator with perpendicular magnetic anisotropy.

To achieve this overarching objective, the study undertook several specific goals. Firstly, it aimed to fabricate high-quality  $\text{WTe}_2$ /CGT heterostructures, maintaining the  $\text{WTe}_2$  thickness consistently below 10 nm. Secondly, it sought to conduct temperature-dependent magneto-transport measurements under different magnetic field configurations in order to identify signatures of magnetic-proximity effect in the  $\text{WTe}_2$  layer.

The experiments showed the presence of magnetic proximity effect, evidenced by measuring the anomalous Hall signal, *i.e* the transversal voltage  $V_{xy}$  under an out-of-plane magnetic field. This signal was enhanced by introducing an annealing process during fabrication, which improves the van der Waals interface quality. The experiments also suggested the influence of spin Hall magnetoresistance (SHMR), necessitating further investigation to determine whether the observed phenomena stem from proximity effects or SHMR.

Looking forward, the long-term objective of this research is to reduce the thickness of  $\text{WTe}_2$  to a monolayer, thereby transforming it into a 2D topological insulator. The ultimate aim is to induce magnetism through proximity effects and to observe the Quantum Anomalous Hall Effect (QAHE), characterized by the quantization of the Hall conductivity in integer multiples of the von Klitzing constant ( $\frac{e^2}{h}$ ). Achieving this would represent a significant advancement in metrology applications, offering new opportunities for the development of quantum devices with tailored magnetic properties.

This manuscript is structured as follows: the first chapter introduces the background concepts related to vdW materials, proximity-induced effects and magneto-transport. This is followed with the description of the device fabrication and the experimental setup. The third chapter presents the results and discussion, focusing on the observed phenomena. Finally, the fourth chapter summarizes the key findings and outlines future research directions.

## 2 Theoretical background

This section describes the theoretical concepts underpinning the phenomena discussed in this thesis.

### 2.1 Van der Waals materials

Since the isolation of graphene in 2004 [NGM<sup>+</sup>04], vdW materials have been at the forefront of fundamental research and applications. These materials present a wide range of behaviors including insulating, semiconducting, metallic, superconducting, topological and the very recently discovered magnetism down to the monolayer limit [MLH<sup>+</sup>10]. Examples include the insulator hexagonal boron nitride (hBN), semiconducting transition metal dichalcogenides (TMDCs), graphene and 2D magnets like CrI<sub>3</sub> and CGT. VdW materials have strong covalent bonds within the atomic plane and weak vdW interlayer forces, making them easy to exfoliate.

The absence of ferromagnetic order in many vdW crystals (such as graphene) has motivated efforts to induce magnetism extrinsically using several methods, including: (i) defect engineering via vacancies, adatoms, grain boundaries or edges, (ii) introducing magnetic species via intercalation or substitution of 2D materials, (iii) utilizing the magnetic proximity effect [GLL<sup>+</sup>17a].

### 2.2 Van der Waals heterostructures

VdW materials are often introduced using graphite as an example, which is composed of stacked sheets of pure carbon. A single atom-thick sheet of carbon extracted from graphite is known as graphene. These atomic sheets resemble cellophane wrap-sticky, flexible, and prone to wrinkling and sticking back onto themselves [BSS85].

2D materials typically exhibit properties distinct from their three dimensional counterpart. For instance, graphene is a zero gap semiconductor, whereas graphite is a semimetal with a band overlap [Jou19]. 2D materials consist of covalently bonded, dangling-bond-free layers that are stacked by VdW forces to form bulk structures [YVC<sup>+</sup>22]. Individual sheets are relatively easy to pull apart from the stack. Thanks to the flat interfaces and the weakness of the vdW forces any combination of these 2D materials can be placed atop each other regardless of differences in crystal structure. Such artificially formed stacks are called vdW heterostructures [GG13]. The in-plane stability of 2D materials ensures the stability of the heterostructure, whereas vdW forces keep the stack together [GG13].

Combining materials with different properties in vdW heterostructures has led to the creation of unique structures, new physical effects, and novel devices [LHW<sup>+</sup>17]. In heterojunctions, the weak vdW forces between the participant materials do not significantly alter the crystal structure but do change the electronic structure [DB20]. Hence, vdW heterojunctions offer the opportunity to engineer new functional materials, allowing charge distribution and magnetic modification (by proximity effect) between monolayers in the stack [DBPL<sup>+</sup>19]. Heterostructures are useful for several reasons, such as using inert materials to protect sensitive ones or combining two vdW materials to exhibit new phenomena not present in individual materials. These properties can be controlled through sample design, electrical means, or adjusting the twist angle between 2D materials [SFK<sup>+</sup>21].

### 2.3 Proximity effects

Stacking atomically thin materials has become a strategy to design new artificial materials in complex vdW heterostructures, combining the pristine properties of selected materials and

imprint others by proximity effects. Materials proximitized to another can acquire properties absent in their pristine form. Historically, this has been observed in superconductor-metal systems, where Cooper pairs penetrate the metal layer over a characteristic coherence depth in the order of tens or even hundreds of nanometers. Owing to the atomically thin nature of vdW materials, short-range interactions like magnetism and SOC can also be imprinted by proximity effects, where the electronic orbitals of the two materials hybridize through the vdW gap [ZMAS<sup>+</sup>18]. This hybridization drastically changes their electronic band structure and spin texture without introducing dopants, impurities or scattering centres [ZMAS<sup>+</sup>18].

Proximity-induced SOC has been predicted and observed in graphene proximitized with layered TMDCs like MoS<sub>2</sub> and WS<sub>2</sub> [GF15, GIAKvW17, BSST<sup>+</sup>17], while proximity-induced magnetism has been demonstrated in graphene and TMDCs combined with vdW magnets like CrSBr, CrI<sub>3</sub> and CrBr<sub>3</sub> [GKD<sup>+</sup>21, ZSL<sup>+</sup>20, LGMS<sup>+</sup>20]. When studying proximity effects, it is essential to consider that the effect is only effective in adjacent layers due to the exponential decay of the hybridization with distance. Therefore, the thickness of the proximitized layer (WTe<sub>2</sub> in this case) must be precisely controlled [LRL<sup>+</sup>22]. Ultimately, the proximity effect extends beyond a single property in bilayer structures. For example, in trilayer systems, the material in the middle can be influenced by both the top and bottom layers.

## 2.4 Hall effect and anomalous Hall effect

In 1879, Edwin H. Hall discovered that when a conductor carrying longitudinal current is placed in a vertical magnetic field, the carriers deflect towards the transverse edges of the conductor, resulting in a transverse voltage. This effect, known as Hall effect (HE), arises due to the Lorentz force acting on the moving carriers in presence of the vertical the magnetic field, which is balanced by a transverse voltage for a steady longitudinal current. [Hal80].

In 1880, Hall found that this effect was more pronounced in ferromagnetic (FM) conductors than in non-magnetic (NM) materials, a phenomenon now termed the anomalous Hall effect (AHE) [Hal81]. Subsequent experiments suggested that the AHE is related to the sample's magnetization  $\vec{M}$  (along the  $z$  direction) [PLK<sup>+</sup>23], leading to an empirical relation for the total Hall effect in FM conductors expressed by the transversal resistivity, *i.e* the Hall resistivity [Pug30]:

$$\rho_{xy} = R_O B_z + R_S M_z, \quad (2.1)$$

where the first term corresponds to the ordinary Hall effect, with  $R_O = -\frac{1}{en}$  representing the Hall coefficient,  $e$  the electron charge, and  $n$  the carrier density. The second term corresponds to the anomalous Hall resistivity, where  $R_S$  is a material-dependent coefficient.

Although the HE and AHE appear quite similar phenomenologically, their underlying physics differs. HE is driven by the Lorentz force on moving electrons under a magnetic field, whereas AHE persists even in the absence of an external magnetic field [YKM<sup>+</sup>04].

The origin of the AHE involves both intrinsic and extrinsic mechanisms [OSN06]. The intrinsic mechanism arises from moving electrons acquiring an "anomalous velocity" perpendicular to the electric field due to the Berry curvature of occupied wave functions. This curvature acts as an effective magnetic field in momentum space, modifying the electrons' equation of motion [XCN10]. This mechanism predicts  $\rho_{xy} \propto \rho_{xx}^2$  [JNM02]. The extrinsic mechanisms include: (i) *skew scattering*, where defects and impurities in the material act as scattering center for the moving electrons. In the presence of spin-orbit coupling (SOC) and ferromagnetism, this

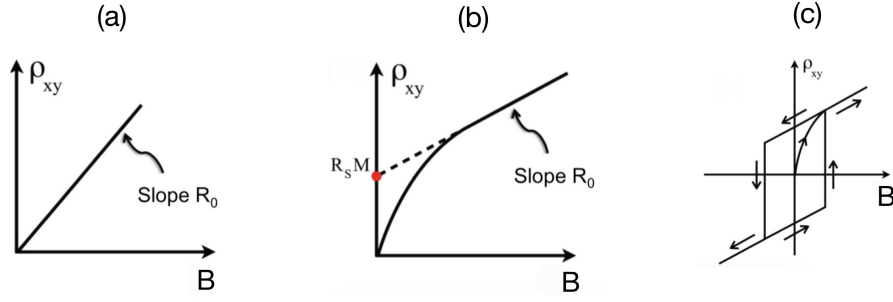


Figure 2.1: Hall resistivity  $\rho_{xy}$  versus external magnetic field  $\vec{B}$ . **a**| Hall effect in non-magnetic materials. **b**| The anomalous Hall effect (AHE) and the Hall effect in magnetic materials. The dashed line extrapolates the linear part to the  $\vec{B} = 0$  limit **c**| Representation of a hysteresis loop due to the AHE. Images adapted from: Ref. [WYH<sup>+</sup>15a]

scattering becomes asymmetric, leading to an unbalanced transverse motion of electrons. This mechanism predicts  $\rho_{xy} \propto \rho_{xx}$  [Smi58]. (ii) *side jump*, where electrons experience different electric fields when approaching and leaving an impurity, resulting in another form of asymmetric scattering. This mechanism predicts  $\rho_{xy} \propto \rho_{xx}^2$  [Ber70].

Figure 2.1(a) illustrates  $\rho_{xy}$  of a NM conductor as a function of a perpendicular magnetic field ( $\vec{B}$ ), displaying a linear dependence characteristic of the HE. In FM conductors, where both the HE and the AHE are present,  $\rho_{xy}$  shows a non-linear behavior with ( $\vec{B}$ ), increasing sharply at low fields due to magnetization saturation, where the AHE becomes noticeable, and then crossing over to a linear region dominated by the HE at higher fields [Figure 2.1(b)]. By extrapolating the linear part to zero field ( $\vec{B} = 0$ ), the intercept on the  $y$ -axis provides the  $R_S M$  term in Eq. 2.1. Essentially, HE is present in all conductors, whereas the AHE is exclusive to magnetic materials [LZQ15].

Experimentally, measurements usually involve sweeping the magnetic field backw and forth, producing a hysteresis loop in  $\rho_{xy}$  vs  $\vec{B}$  for materials exhibiting AHE [Figure 2.1(c)]. This loop reflects the magnetization component (second term of Eq. 2.1), characterized by an hysteretic behaviour below a certain coercive field ( $H_C$ ), alongside a constant slope from the HE (first term of 2.1) [WYH<sup>+</sup>15a].

In this thesis, the AHE is used to identify proximity-induced magnetism in vdW materials. The atomically thin nature of vdW materials allows for imprinting short range interactions, such as magnetic exchange interaction and SOC, by stacking them vertically. Here, (semi)metallic WTe<sub>2</sub> is combined with the insulating FM material Cr<sub>2</sub>Ge<sub>2</sub>Te<sub>6</sub> (CGT) in a vdW heterostructure, and temperature-dependent magneto-transport experiments are performed. Since the CGT layer is expected to be highly insulating, the observation of AHE in the CGT/WTe<sub>2</sub> stack would indicate magnetism in WTe<sub>2</sub> induced by proximity effects. However, one has to take into account that, even though the observation of the AHE signals could be ascribed to magnetic proximity effects, other phenomena unrelated to proximity effects, such as spin Hall magnetoresistance (SHMR), can lead to similar results.

#### 2.4.1 Quantum anomalous Hall effect in magnetic topological insulators

Topological insulators (TIs) represent a state of matter characterized by insulating bulk properties and conductive boundary states that preserve time-reversal symmetry. These boundary states give rise to phenomena such as the quantum spin Hall effect (QSHE), where the edges

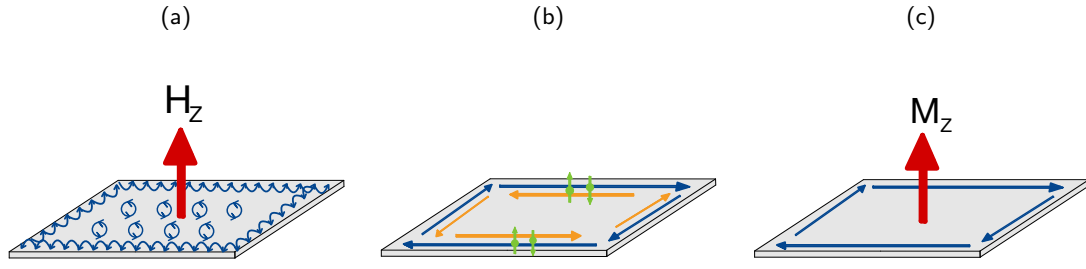


Figure 2.2: Illustration of the edge states in a| QHE, b| QSHE and c| QAHE.

of a 2D TI support spin-polarized currents, as shown in [Figure 2.2b]. These edge states consist of pairs of counter-propagating chiral channels, which are channels with opposite directions of propagation, characterized by unidirectional movement without scattering or back-scattering. These channels exhibit resistance to non-magnetic impurities [BAG<sup>+</sup>21]. When time-reversal symmetry is broken by introducing magnetism into TIs, novel quantum phenomena such as the QAHE can potentially emerge [DYS<sup>+</sup>20].

The QAHE, which requires materials with broken time-reversal symmetry, is characterized by the presence of dissipationless charge currents at the edges and quantized Hall resistance, without the need for an external magnetic field [Figure 2.2c], unlike in the quantum Hall effect (QHE), where a large external magnetic field is required [WYH<sup>+</sup>15b] [Figure 2.2a].

Magnetic doping, such as the introduction of chromium impurities into (Bi,Sb)<sub>2</sub>Te<sub>3</sub> films, has been shown to induce QAHE [CZF<sup>+</sup>13]. However, this method introduces disorder, degrading the electronic properties of the material and limiting the observation of Hall quantization with metrological precision to mK temperatures. An alternative approach involves inducing magnetism through magnetic proximity effects. Even though efforts have been made to utilize magnetic proximity-induced effects to observe the QAHE in systems combining 3D magnets with 3D TIs [BAG<sup>+</sup>20], these interfaces often suffer from intermixing of materials and alloying. This is why 2D materials are preferred; they offer atomically sharp interfaces, devoid of defects and intermixing, and present opportunities for various combinations due to the abundance of 2D materials with different physical properties. For example, magnetism can be induced in monolayer of WTe<sub>2</sub>, a topological insulator, using CGT as the magnetic layer. This method can potentially induce magnetism without introducing impurities, potentially facilitating the observation of anomalous Hall quantization at higher temperatures [BAG<sup>+</sup>21].

## 2.5 Spin Hall magnetoresistance

Magnetoresistance (MR) is a property of materials that causes their electrical resistance to change in response to an applied magnetic field. This phenomenon is observed when the flow of electric current through a material is affected by the presence of a magnetic field, leading to an increase or decrease in resistance.

Recently, a fundamentally different type of MR, caused by the proximity of a metallic film, with high SOC, attached to an electrically insulating magnet, has been reported. Even though the conduction electrons in the metallic film cannot enter the magnetic insulator, the bilayer's resistance (of both materials in contact) reflects the magnetization of the insulating magnet



[NAC<sup>+</sup>13].

In this thesis, this phenomenon, known as spin Hall magnetoresistance (SHMR), could be observed due to the interface of a semiconducting magnet CGT and the semimetallic WTe<sub>2</sub>, which has strong SOC.

Spin transport and charge transport phenomena are interconnected. For example, the spin Hall effect (SHE) refers to the conversion of an electric current into a transverse spin current, whereas the inverse spin Hall effect (ISHE) refers to the reciprocal effect, namely the conversion of an injected spin current into a transverse electric current or voltage. In a high-symmetry material, the directions of electric-current flow ( $\vec{J}_e$ ), spin-current flow ( $\vec{J}_s$ ), and spin current polarization ( $\vec{\sigma}$ ) are perpendicular to one another.

The SHMR is based on the simultaneous operation of the SHE and its reciprocal, the ISHE. Considering a heterostructure made up of an insulating magnet on top of a metallic thin film exhibiting strong SOC: When an electric current ( $\vec{J}_e$ ) is applied along the film plane, it induces a spin current  $\vec{J}_s$  in the meta, due to the SHE. This spin current travels perpendicular to the film surface with spin polarization  $\vec{\sigma}$  parallel to the surface, as shown in Figure 2.3 [CTN<sup>+</sup>13].

The interface between both materials results in interfacial spin mixing, leading to the spin-angular-momentum exchange between the magnetization ( $\vec{M}$ ) in the magnet and conduction-electron spin polarization  $\vec{\sigma}$  in the metal. Spin-flip scattering is activated when  $\vec{\sigma}$  and  $\vec{M}$  are not collinear, as shown in Figure 2.3. Part of the spin current is absorbed by the magnetization as spin-transfer torque. The absorption is maximized when  $\vec{M}$  is perpendicular to  $\vec{\sigma}$  and there is no absorption when  $\vec{M}$  is parallel to  $\vec{\sigma}$  [NAC<sup>+</sup>13, YLW<sup>+</sup>18]. The unabsorbed spin current is reflected back into the metal film, inducing an electric current from the ISHE. This additional electric current, due to the combination of SHE and ISHE is always parallel to the original one, in agreement with the Onsager relation [LSN<sup>+</sup>19].

Therefore, the conductivity increase due to SHE and ISHE is expected to be maximum (minimum) when  $\vec{M}$  is perpendicular to  $\vec{J}_e$  [Figure 2.3a (parallel Figure 2.3b)], because  $\vec{J}_e$  is perpendicular to  $\vec{\sigma}$ . Consequently, the metallic film's resistance is affected by the magnetization direction in the magnet, giving rise to the SHMR. SHMR is an interface phenomenon and critically depends on the quality of the interface, occurring only on the length scale of the spin diffusion length [KTO<sup>+</sup>24].

## 2.6 Differentiating magnetic proximity effect and spin Hall magnetoresistance

In the scenario of SHMR and AHE, the longitudinal and transverse resistances, when applying the current in the x-direction, are given by Eq. 2.2a and Eq. 2.2b.

$$R_{xx} = R^{AMR} \cos^2(\phi) \sin^2(\theta) + R^{SHMR} \sin^2(\phi) \sin^2(\theta) + R_0, \quad (2.2a)$$

$$R_{xy} = R_H^{SHMR} \sin(2\phi) \sin^2(\theta) + R_{AHE}^{SHMR} \cos(\theta) + R_{HE} H_z. \quad (2.2b)$$

Here,  $R_0$ ,  $R^{SHMR}$ , and  $R^{AMR}$  represent the magnetization direction-independent resistance, the modulation due to SHMR, and the anisotropic magnetoresistance (AMR)—the change in resistance of a ferromagnetic material when its magnetization is rotated relative to the current direction.  $R_H^{SHMR}$ ,  $R_{AHE}^{SHMR}$ , and  $R_{HE}$  denote the transverse manifestation of SHMR, the SHMR-induced AHE-like resistance, and the ordinary Hall effect resistance, respectively.  $\theta$  and  $\phi$  are the polar and azimuthal magnetization angles. It is evident that the transverse SHMR and the SHMR-induced AHE are analogous to the planar Hall resistance

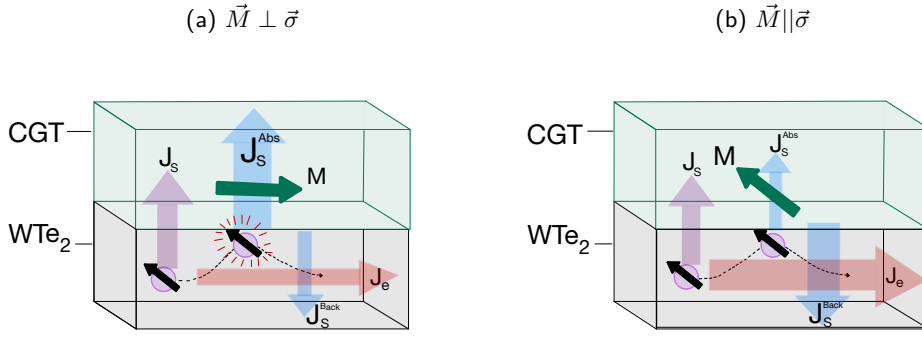


Figure 2.3: Illustrations of the geometric relation between the flow of electrons and accumulated spins in  $\text{WTe}_2$  and the magnetization in the magnetic semiconductor CGT. In the case of a) absorption and b) reflection

( $R_{PHE}$ )-voltage induced perpendicular to the current direction in a ferromagnetic material when an in-plane magnetic field aligns the magnetization, caused by AMR- and anomalous Hall resistance ( $R_{AHE}$ ) in conducting ferromagnets by symmetry, as shown in Eq. 2.3.

$$R_{xy} = R_{PHE} \sin(2\phi) \sin^2(\theta) + R_{AHE} \cos(\theta). \quad (2.3)$$

The challenge distinguishing whether one is observing SHMR, a pure spin current phenomenon in bilayer structures, or AMR, which can only originate from proximity effects.

One method is to study the angle dependence of the resistance in the three different planes [LTAS14]. In the scenario of a strong spin-orbit coupling metal with high symmetry structure and a magnetic insulator, the in-plane ( $xy$ -plane containing the spin polarization direction and the current flowing in the  $x$ -axis) field sweep cannot distinguish between SHMR and AMR, since both phenomena depend on the orientation of the magnetization ( $\vec{M}$ ) in this plane. If  $\vec{M}$  is rotated by an angle  $\theta$  in the  $xy$ -plane, both SHMR and AMR change simultaneously, entangling the two effects [Figure 2.4a]. In contrast, as shown in Figure 2.4b, if  $\vec{M}$  is rotated by an angle  $\alpha$  in the  $xz$ -plane, SHMR should remain constant since  $\vec{M}$  and  $\vec{\sigma}$  are always perpendicular. Thus, any resistance change can be attributed to AMR. Conversely, if  $\vec{M}$  is rotated in the  $yz$ -plane by an angle  $\beta$ , AMR should remain constant since the charge current ( $\vec{J}_e$ ) is always perpendicular to  $\vec{M}$ . Therefore, any resistance change can be attributed to SHMR [Figure 2.4c].

In an ideal symmetric crystal, changing the axis along which the current is applied should not change the resistance behavior. However, for  $\text{WTe}_2$ , due to its low symmetry, the spin texture is not necessarily perpendicular to the applied charge current. Consequently, applying current along different directions can yield different resistance behavior.

In low-symmetry crystal, the spin polarization may not be perpendicular to the applied current and can orient in any direction, contributing to resistance changes in various planes. Consider a scenario where the spin polarization lies in the  $xy$ -plane, with components in both axes. When a current is applied along the  $x$ -axis (assuming this is a crystallographic axis), rotating the magnetic field by angle  $\alpha$  in the  $xz$ -plane results in resistance changes attributable to both SHMR and AMR, unlike the single contribution of AMR in high symmetry case.

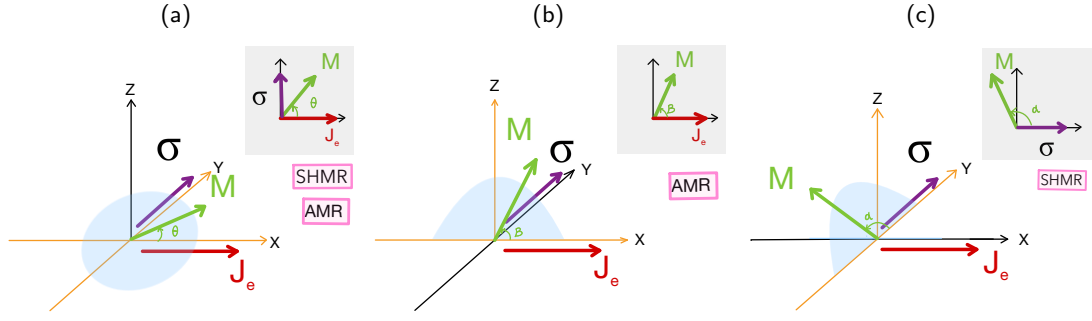


Figure 2.4: Illustration of geometric relation between the the charge current ( $J_e$ ), the spin polarization ( $\sigma$ ), and magnetization ( $M$ ), in the case of a high symmetry crystal. Spin Hall magnetoresistance (SHMR) or anisotropic magnetoresistance (AMR), that can take place by the rotation of  $M$  in each plane. in each plane are highlighted in pink the phenomenon affecting the resistance

This complexity makes it challenging to differentiate between SHMR and AMR. Nonetheless, applying the current in the other crystallographic direction ( $y$ -axis) should result in a different resistance behaviour. By comparing changes along both directions, it becomes possible to discriminate between the phenomena. Changes in resistance behavior depending on the current axis could be attributed to SHMR, as AMR effect on the resistance should remain unchanged with axis changes. AMR depends only on the angle between the current direction and magnetization, which are consistent for both crystallographic axes. In contrast, the SHMR depends on the SHE and the angle of spin polarization, implying that the observed change on the resistance behavior when changing the current axis could be due to the SHMR.

This thesis initiates the exploration of this process by measuring the changes of the resistance as a function of the in plane ( $xy$ -plane) rotation of the magnetic field for two perpendicular current directions. Since a Raman spectroscopy [SPW<sup>+</sup>16] has not been performed in the device to determine the crystallographic axes, it cannot be confirmed yet that the current directions correspond to crystallographic axes. However, for simplicity, they will be referred to as such hereafter. As previously mentioned, with the in-plane rotation of  $B$ , conclusions regarding the dominant phenomenon cannot be drawn, as both contribute. The objective is to observe if there is a variation in resistance behavior when applying current along different axis. Finally, measurements corresponding to the other planes have been started to complete the study and reach a definitive conclusion.

### 3 Experimental background

This section introduces the vdW materials that form the heterostructure:  $\text{WTe}_2$ , covered with CGT, and hBN on top of it to protect the heterostructure against oxidation. It further presents the device fabrication process and describes the experimental setup for magnetotransport measurements.

#### 3.1 Materials utilized for heterostructure fabrication

##### 3.1.1 Hexagonal boron nitride

Boron nitride (BN) is a chemical compound isoelectronic and isostructural to carbon, composed of boron and nitrogen atoms. Hexagonal boron nitride (hBN) is the most common form

of BN, and its crystalline structure resembles graphite. hBN features a layered structure with strong in-plane covalent bonds between boron and nitrogen atoms and interlayer vdW forces. Although structurally similar to graphene, hBN is a wide bandgap material. It is also chemically inert in a wide variety of acids, solvents, and oxidizers [BGR16]. Owing to its high chemical resistance and thermal stability, hBN is used in this study as a chemically inert coating [LGZ<sup>+</sup>13] of the WTe<sub>2</sub>-CGT heterostructure to protect it against oxidation.

### 3.1.2 The van der Waals magnet Cr<sub>2</sub>Ge<sub>2</sub>Te<sub>6</sub>

The discovery of long-range ferromagnetic ordering in vdW materials like CGT has opened new avenues for exploring low-dimensional magnetism and potential applications within novel memory, computing, and quantum computing [GLL<sup>+</sup>17b]. CGT is a semiconducting ferromagnet with a bulk Curie temperature  $T_c$  of about 63 K, which decreases to about 30 K in the bilayer case [THP<sup>+</sup>23]. It exhibits perpendicular magnetic anisotropy and nearly ideal ferromagnetic behavior, making it an excellent system to investigate fundamental magnetic phenomena. [ZZS<sup>+</sup>16].

The first studies on bulk crystals of CGT date back to 1995 [CBOA95]). Intensive research started in 2017, when long-range magnetic order was demonstrated in bilayer CGT using magneto-optic Kerr microscopy [ZZS<sup>+</sup>16]. Prior to this, the persistence of long-range ferromagnetic order in the 2D regime was uncertain due to the susceptibility of 2D ferromagnetism to thermal fluctuations. Renewed interest in CGT and other related vdW magnets arose in part from the experimental confirmation that in the 2D limit, magnetic anisotropy can overcome thermal fluctuations, thereby stabilizing the long-range magnetic order [GLL<sup>+</sup>17a].

CGT's crystal structure consists of layers of Cr atoms sandwiched between Te and Ge atoms, with each layer having a thickness of  $\sim 6.9\text{\AA}$  [XCO<sup>+</sup>17]. CGT flakes degrade in ambient conditions due to oxidation, forming a  $\sim 5\text{nm}$  thick oxide layer. Recent experiments suggest that up to 10 nm of the crystal surface exposed to air becomes non-magnetic [GLL<sup>+</sup>17a]. To prevent this, CGT is exfoliated and stacked in a glove box with an inert atmosphere of Ar containing very low concentration (below 0.1 p.p.m) of O<sub>2</sub> and H<sub>2</sub>O.

The proximity effect, and thus the induced magnetism, is driven by the CGT layer in direct contact with WTe<sub>2</sub>. Therefore, precise control of the number of layers in the CGT flakes is not required, as long as the CGT flake is homogeneous and larger than the WTe<sub>2</sub> flake, in order to shield the later from air exposure, as it is more sensitive than CGT.

### 3.1.3 Tungsten ditelluride

Tungsten ditelluride (WTe<sub>2</sub>) belongs to the family of transition metal dichalcogenides (TMDCs), layered materials of the form MX<sub>2</sub>, where M is a transition metal atom from groups IV (Ti, Zr, Hf and so on), V (for instance V, Nb, or Ta) or VI (Mo, W etc.) with a partially filled d-shell, and X is a chalcogen atom (such as S, Se or Te) [Eft17]. M and X atoms are strongly linked through covalent bounds to form 2D layers. Two adjacent sheets of chalcogen atoms are separated by a sheet of transition metal atoms, and the actual "monolayer" is composed of an atomic trilayer structure. The interaction among these monolayers is the weak vdW interaction, in analogy to graphite. TMDCs like MoS<sub>2</sub>, WS<sub>2</sub>, MoSe<sub>2</sub> and WSe<sub>2</sub>, are notable 2D semiconductors with a direct band gap of  $\sim 1\text{ eV}$  in the monolayer form, strong SOC, and light-matter interaction, making them highly attractive for electronic and opto-electronic applications [MOP<sup>+</sup>17],[NMCN16].

TMDCs exist in several structural phases resulting from the different symmetry between the

three atomic planes (chalcogen-metal-chalcogen) that form the monolayer of these materials. The most stable phases are characterized by either a trigonal prismatic (2H) structure, with stacking sequence ABA where the top and bottom chalcogen atoms occupy same position, or an octahedral (1T) structure with an ABC stacking sequence where top and bottom chalcogen atoms slightly distorted [HDK<sup>+</sup>18].

WTe<sub>2</sub> is a TMDC that is stable in the orthorhombic Td phase. Bulk WTe<sub>2</sub> is a Weyl semi-metal [LWH<sup>+</sup>17, AAF<sup>+</sup>21] and becomes a 2D topological insulator in the monolayer form [QLFL14]. Monolayer WTe<sub>2</sub> is a candidate for realizing the QAHE when proximitized to an insulating magnetic material. WTe<sub>2</sub> is also known for its unique electronic transport properties such as non-saturating positive large magneto-resistance (MR) in bulk, which is attributed to a nearly perfect balance between electron and hole concentrations. MR is typically reported as  $\frac{\rho(B)-\rho(0)}{\rho(0)}$ , and  $\rho(B)$  is the resistivity in an applied magnetic field  $B$ . Positive MR is observed in metals, semiconductors and semimetals, while magnetic materials exhibit negative MR [AXF<sup>+</sup>14]. Experiments show that the imbalance of carrier densities caused by thickness reduction plays an important role in suppressing the positive MR, while the non-saturating remains largely unaffected [ZKW<sup>+</sup>21]. Many other peculiar electronic properties have also been observed such as small Fermi surface anisotropy [WWL<sup>+</sup>19], ferroelectricity and superconductivity [FZP<sup>+</sup>18, FWC<sup>+</sup>18].

## 3.2 Device fabrication

The fabrication of devices involves four main steps, detailed below.

### 3.2.1 Pre-patterned contacts defined by electron beam lithography

To avoid damaging the vdW crystals, lithography steps involving exposure to chemicals, are carried out before flake transfer. The initial design and fabrication of contacts are done through electron beam (e-beam) lithography, followed by a deposition of Ti and Pd (or Au). The device configuration is based on a Hall bar geometry with eight contacts, two of them defining current channel and six for measuring longitudinal or transverse voltage, as depicted in Figures 4.1 (a) and (d).

The pre-patterned Hall bars are fabricated on a 440 nm SiO<sub>2</sub>, cleaned with O<sub>2</sub> plasma. E-beam lithography involves coating the sample with a resist mask, which is then exposed to the electron beam that defines the contacts. After exposure and development of the resist, metallization of the contacts was done using e-beam evaporation of 5 nm of Ti and 30 nm of Pd. Finally a lift-off process with acetone was used to remove the non-exposed resist mask.

### 3.2.2 Mechanical exfoliation of the source materials

The first step in the fabrication process involves the mechanical exfoliation of CGT and WTe<sub>2</sub> inside the glove box in order to prevent degradation of the exfoliated flakes. The well-established *scotch-tape* method [GLQ<sup>+</sup>18] is used for exfoliation. The source material is transferred to adhesive tape (Nitto or Scotch tape), peeled off several times and then transferred onto an insulating substrate of SiO<sub>2</sub>. In this thesis p-doped Si substrates coated with 440nm of SiO<sub>2</sub> are used. The substrates with exfoliated material are inspected with an optical microscope to estimate the thickness of the exfoliated flakes by analyzing the optical reflectivity of blue, green and red channels under bright-field mode and determine the surface homogeneity of the flakes under dark-field mode.

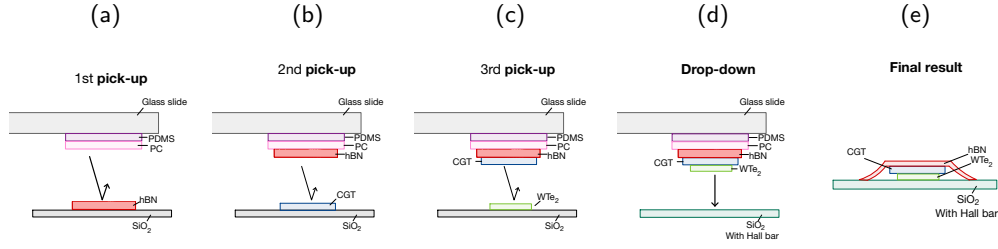


Figure 3.1: Schematic process flow for assembly of van der Waals heterostructures by pick-up and drop-down.

The aim in this work is to maximize the proximity-induced magnetism by the CGT layer, targeting thin  $\text{WTe}_2$  layers about 6-10 nm thick and approximately  $10 \mu\text{m} \times 3 \mu\text{m}$  in size. Optical images of some of the exfoliated  $\text{WTe}_2$  and CGT flakes used in the final devices are shown in Figures 4.1 (b) and (e) and 4.1 (c) and (f), respectively. hBN is also exfoliated and used as a capping layer to prevent degradation of the CGT- $\text{WTe}_2$  heterostructure.

### 3.2.3 Heterostructure stacking and deterministic transfer

The vdW heterostructure is fabricated using a deterministic dry transfer and pick-up technique, as outlined in [Figure 4.5]. A polydimethylsiloxane (PDMS) block coated with a thin layer of polycarbonate (PC) is used as a viscoelastic stamp to pick up and release the selected flakes. The stamp is mounted on a glass slide and fixed to an x,y,z micromanipulator. The substrates with the selected flakes are mounted on a microscope stage with a heater to control the stage temperature, thus adjusting the viscosity and stickiness of the PC [PGJ+16] stamp. The stamp is then approached gently to the target flake and picks it up. This process is repeated in order to stack the hBN/CGT/ $\text{WTe}_2$  sequence and then dropped it onto a  $\text{SiO}_2$  substrate with the pre-patterned electrical contacts in the Hall bar geometry. Specifically, the pick-up process for the hBN flake involves heating the stage to  $T=100^\circ\text{C}$ , followed by a 5-minute heating step at  $T=140^\circ\text{C}$ , and then cooling back to  $T=100^\circ\text{C}$ . Once the hBN is picked up, the chip with the exfoliated crystals of CGT is placed on the microscope stage and the CGT flake picked-up using the the hBN flake. Finally, the  $\text{WTe}_2$  flake is picked up by the hBN/CGT stack and transferred onto the pre-patterned Hall bar contacts, by heating up the stage up to  $T=200^\circ\text{C}$  to melt the PC. Residues of PC on the finished device are cleaned by soaking the chip first in chloroform for 20 s and then in isopropanol for 90 s.

### 3.2.4 High vacuum annealing

After fabricating the device, the final step before starting the measurements process is annealing the device in a high vacuum. The purpose of annealing is to improve the interface quality between CGT and  $\text{WTe}_2$  and between the whole heterostructure and the pre-patterned contacts. Vacuum annealing is a heat treatment process conducted in an environment devoid of air or any other gas. It involves heating to a specific temperature, maintaining that temperature for a set period, and then allowing controlled cooling.

The annealing temperature as well as the temperature ramps must be chosen carefully to prevent degradation of the the constituent materials. Some devices were annealed at  $220^\circ\text{C}$  for 3 hours. After initial measurements, they were annealed again at  $280^\circ\text{C}$  for 3 hours. Finally,

devices with thicker CGT layers underwent annealing at 330 °C for 3 hours. In all the annealing processes, a ramp rate of 3 °C/min for heating up and cooling down was used.

### 3.3 Magneto-transport measurement set-up

In the magneto-transport measurements, the devices, previously wire-bonded, are fixed to a chip carrier to establish electrical connections. The measurements were carried out in two setups, each comprising a closed-cycle cryostat with a base temperature of 6 K. In one of the setups (setup 1), the current was supplied using a Keithley current source operating at an alternating current (AC) frequency of  $f_{ac} = 177$  Hz, and the voltage measured with a lock-in amplifier from Stanford Research Systems. The second setup (setup 2) used a Keithley current source and nanovoltmeter operating in delta mode. Here, the current source is alternating the current polarity at a frequency of  $f_{ac} = 1$  Hz and the voltage is measured via the triggered nanovoltmeter.

Additionally, the two setups differ in their magnetic field capabilities. In setup 1 the electro-magnet can generate magnetic fields up to 1.4 T, while setup 2 operates up to 0.6 T. Setup 1 also features a motorized magnet (for rotation), as opposed to the manual operation of setup 2. Both setups allow the orientation of the magnetic fields to be adjusted from out-of-plane to in-plane, offering flexibility in experimental conditions. Experiments were fully computer-controlled via a Labview software interface, ensuring precise and automated measurement processes.

## 4 Results and discussion

In this section, the results obtained from the experimental analysis are presented and discussed, organized into several subsections. An overview of all the analyzed chips and the annealing effects on the device resistances and is provided first, followed by a discussion on the increase in critical temperature. The variation of longitudinal and transverse resistances as a function of magnetic field (along the z-axis,  $B_z$ ) and temperature is then examined. Finally, the angular dependence of the magnetic field in the plane is investigated to determine whether the observed phenomena are due to proximity effects or the SHMR.

In each subsection, rather than presenting the results for every fabricated chip, the results of a single representative chip are showcased. The selected chip exemplifies the performance and characteristics observed across all other chips, allowing for a clear and concise understanding of the overall results without redundancy.

### 4.1 Device overview and proximity phenomena analysis

Figure 4.1 provides an overview of the devices analyzed in the study. Six devices were fabricated and measured, labeled in chronologically from 1 to 6. The initial investigation focused on the influence of the  $\text{WTe}_2$  thickness on the manifestation of AHE within the heterostructures. Importantly, the AHE due to proximity effects and the SHMR present very different thickness dependencies. While the AHE must increase monotonically with reducing  $\text{WTe}_2$  thickness, the SHMR is expected to show a non-monotonic behaviour. The SHMR must tend to zero at both large and small thickness limits, reaching maximum magnitude at a  $\text{WTe}_2$  thickness of about twice the spin relaxation length in  $\text{WTe}_2$ , which has been estimated to be approximately 8 nm [ZKZ<sup>+</sup>20].

Anomalous Hall signal were observed in all devices, with two notable exception. Device 2, characterized by the thickest  $\text{WTe}_2$  layer and the thinnest CGT layer, did not exhibit an AHE



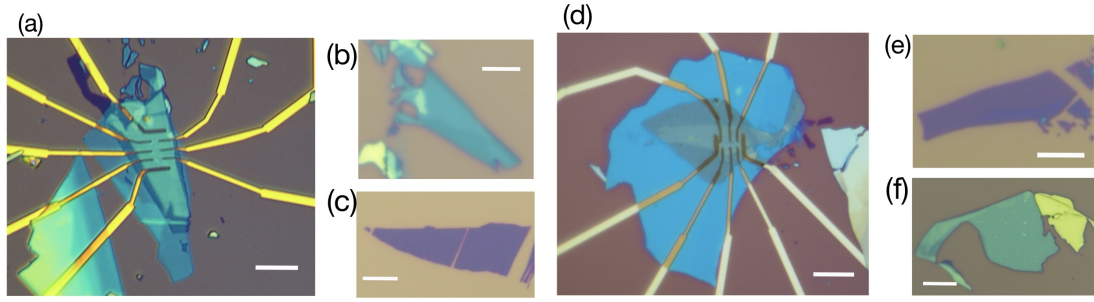


Figure 4.1: a| Device 2: Heterostructure of  $\text{WTe}_2$ , CGT, and hBN. b| Flake of  $\text{WTe}_2$  in device 2. c| Flake of CGT in device 2. d| device 5: Heterostructure of  $\text{WTe}_2$ , CGT, and hBN. e| Flake of  $\text{WTe}_2$  in device 5. f| Flake of CGT in device 5. The white line indicates a length of 10  $\mu\text{m}$ .

signal. Similarly device 3 which has a relatively thick layer of  $\text{WTe}_2$ , also did not show an AHE signal.

	Device 1	Device 2	Device 3	Device 4	Device 5	Device 6
No AHE	220 °C	220°C, 280°C	220°C, 280°C, 330°C	220°C		280°C
AHE	280 °C			280°C	280 °C	330°C

Table 4.1: Overview of the annealing temperatures at which the fabricated devices exhibited (or did not exhibit) an AHE signal.

A correlation between the thickness of the CGT layer and the requisite annealing temperature was observed, as devices with thicker CGT layers necessitated higher annealing temperatures to observe AHE signal. Specifically, while devices exhibiting AHE signal underwent annealing at 280 °C, devices with thicker CGT flakes, such as device 6, required elevated annealing temperatures of 330 °C to observe it, as shown in 4.1.

## 4.2 Effect of annealing on device resistances

In device 4, the first annealing process was performed at  $T_{\text{an}} = 220$  °C for three hours. At low temperatures, the measured resistance of individual CGT flakes is orders of magnitude larger ( $\text{M}\Omega$ ) [KTO<sup>+</sup>24] compared to the resistance of the  $\text{WTe}_2$ /CGT bilayer, indicating that most of the applied charge current to the  $\text{WTe}_2$ /CGT bilayer flows through  $\text{WTe}_2$ .

Moreover, the longitudinal resistance  $R_{xx}$  was measured as a function of temperature [Figure 4.2a], showing semiconductor behavior (resistance decreases with temperature) on one side of the sample, and metallic or semi-metallic behaviour (resistance increases with temperature) on the other side, consistent with the behaviour of  $\text{WTe}_2$ . The difference in resistance between different WTe<sub>2</sub> sides was observed in several devices. This could be ascribed to inhomogeneities in the  $\text{WTe}_2$  flake, or oxidation due to barging encapsulation.

A second annealing process was conducted at a higher temperature  $T_{\text{an}} = 280$  °C for three hours. The aim of increasing the annealing temperature was to create a higher quality vdW interface between CGT and  $\text{WTe}_2$ , since no AHE signal was observed after the initial annealing. The temperature dependence of  $R_{xx}$  was measured again [Figure 4.2b], focusing on the metallic side of the sample, showing a slight decrease in the resistance magnitude and changes in the device behavior at low temperatures, where the resistance does not decrease as the temperature decreases.



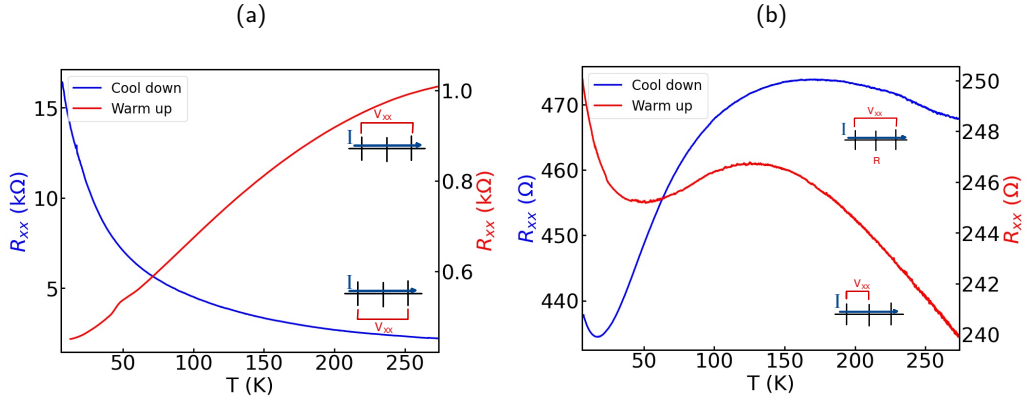


Figure 4.2: Temperature dependence of  $R_{xx}$  after the annealing at a)  $T_{an} = 220$  °. and at b)  $T_{an} = 280$  °C. In blue the cool down measurements and in red the warm up. Graphical representation of the contacts involved in each measurement.

### 4.3 Magneto-transport measurements

Magneto-transport measurements of the transverse resistance  $R_{xy}$  for Device 5 are presented in Figure 4.3a, showing clear hysteresis loops as a function of out-of-plane magnetic field for different temperatures. Notably, the AHE-like hysteresis loop persists up to a critical temperature of  $T_c = 90$  K, in contrast with the pristine  $T_c = 63$  K observed in bulk CGT. This effect was observed in four of six devices after annealing at 280 °C (330° for thicker samples) with a  $T_c$  summarized in Table 4.2. The average critical temperatures across all devices is calculated to be  $T_c = 96.5$  K, indicating a significant 53% increase from the  $T_c$  of pristine CGT [THP+23]. The origin of this increase can be due to the SOC of the  $WTe_2$  stabilizing the ferromagnetic order in CGT *at the interface* with  $WTe_2$ , since proximity effects are not expected to extend beyond one or two atomic layers and modify the  $T_c$  of bulk CGT.

Device 1	Device 4	Device 5	Device 6
120 K	90 K	90 K	86 K

Table 4.2: Critical temperature ( $T_c$ ) of devices exhibiting AHE signal

Figure 4.3b provides additional insights into the magnetic behavior, showing the magnitude of the remanent signal at zero magnetic field and the coercive field, as obtained from the hysteresis loops. At  $T = 10$  K, the coercive field is approximately 200 mT, contrasting sharply with the negligible coercivity observed in pristine CGT [KTO+24]. Analysis of Figure 4.3b allows for the determination of  $T_c$  based on the temperature above which the remanent signal and coercive field are no longer perceptible.

Furthermore, Figure 4.3c reveals a linear background attributed to the ordinary Hall effect, which can be fitted with a linear function; the green marks the hysteresis loop extension. Figure 4.3d illustrates the temperature dependence of the charge carrier density, derived from the slope of the linear fit using  $n = \frac{1}{R_H e}$ , where  $R_H$  is the Hall coefficient ( $R_H = \text{slope} / 1000 [\Omega/T]$ ) and  $e$  is the charge of the electron. The sign of the carrier density is by convention positive for holes and negative for electrons (complementary information in Annex B). In 4.3d, it is observed that the number of carriers decreases as the temperature decreases, which is expected as less thermal energy is supplied to the system. Moreover, magneto-resistance measurements, as

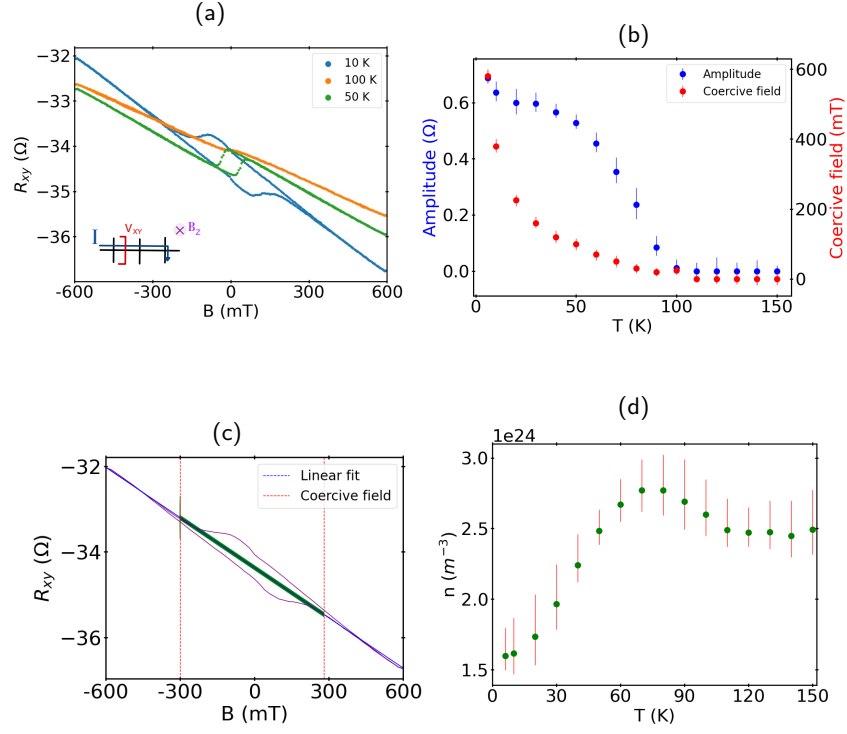


Figure 4.3: a| Transverse resistance ( $R_{xy}$ ) as a function of out-of-plane magnetic field ( $B_z$ ) for different temperatures. The curves are plotted with an offset, for raw data go to Appendix. Bottom left a scheme of the contact design. b| Coercive field (red), and amplitude at 0 mT (blue) as a function of the temperature. c|  $R_{xy}$  as a function of  $B_z$  for  $T=10$  K. Blue dashed line corresponds to the linear fit, red dashed line marks where the hysteresis loop closes, and green indicates the width of the hysteresis loop. d| charge carrier density as a function of the temperature.

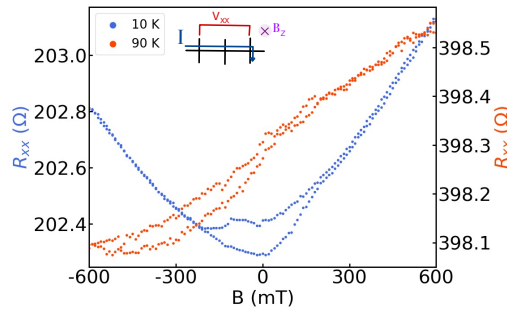


Figure 4.4: Longitudinal resistance ( $R_{xx}$ ) as a function of out-of-plane magnetic field ( $B_z$ ) for different temperatures. Top left a scheme of the contact design

shown in Figure 4.4, exhibit a parabolic behavior in  $R_{xx}$ , as expected since magneto-resistance mechanisms lead to a symmetric (even) response with the magnetic field. This behavior persists up to  $T_c$ , beyond which the parabolic MR vanishes, leaving mainly the linear dependence originating from a residual  $R_{xy}$  component, which is also present at low temperatures (300 mΩ at 10 K and 400 mΩ at 90 K).

#### 4.4 In-plane magnetic field angular dependence

$R_{xy}$  from device 5 was measured as a function of the in-plane magnetic field angle  $\phi$ , with  $\phi=0$  when  $B$  parallel to  $I$ . The data was symmetrized and antisymmetrized to minimize the cross contribution of longitudinal and transverse resistances. The symmetric component is associated to  $R_{xx}$ , whereas the antisymmetric component corresponds to  $R_{xy}$ . The angular dependence in resistance was measured for two perpendicular current directions, i.e along the long and short sides of the device.

##### 4.4.1 First axis

For the first axis, where the current flows along the x-axis, that is, along the long side of the device [see Figure 4.5e]. Figure 4.5a shows the symmetric component of the resistance as a function of the angle of the in-plane field at  $T=10$  K for selected magnetic field magnitude. The data was fitted using equation 4.1 with two free parameters: the amplitude ( $A$ ) and a field-dependent offset ( $D$ ). Figure 4.5b shows  $A$  as a function of  $B$ . The saturation of  $A$  at around 600 mT, when the magnetization rotates to the plane, demonstrates the magnetic origin of the signal. Figure 4.5c shows  $A$  as a function of temperature for the indicated  $B$ , with a similar temperature dependence as in 4.3.

Figure 4.5d presents the antisymmetric part of the resistance as a function of the angle of the in-plane field at  $B = 1400$  mT for different temperatures. The data were fitted using equation 4.2 with three fitting parameters: the amplitude ( $A'$ ), the offset ( $D'$ ), and frequency ( $\nu$ ). This fitting approach was chosen because the signal does not follow a  $\sin(2\phi)$  modulation, as one would expect from equation 2.2b. This suggests that the antisymmetric  $R_{xy}$  component is caused by a small out-of-plane component ( $B_z$ ), probably due to sample misalignment, leading to AHE and ordinary HE. As a consequence,  $\theta \neq 0$ , changes with  $\phi$ , being 0 at  $\phi = 0$  and  $\phi = 180$ , and reaching maximum (minimum) at  $\phi = 90$  ( $\phi = 270$ ).

$$f_{Sym} = (A \cos(c_1 \cdot \phi + c_2))^2 + D = \frac{A^2}{2}(1 + \cos(2c_1 \cdot \phi + c_2)) + D, \quad (4.1)$$

$$f_{Antisym} = A' \cos(\nu \cdot \theta + c_3) + D', \quad (4.2)$$

where  $c_1$ ,  $c_2$  and  $c_3$  are constants.

Figure 4.5e shows the amplitude of the fit as a function of temperature (for 1400 mT), increasing and peaking around  $T = 90$  K, which corresponds to the  $T_c$  identified in the previous section. The high amplitude above  $T_c$  is likely due to the AHE and primarily the HE. Figure 4.5f shows the transition for  $R_{Antisym}$  from an AHE-like behavior to a HE at a similar saturation field (600 mT at 10 K). For temperatures above  $T_c$ , there is only a linear field dependence. At low temperatures and  $B < 600$  mT, an AHE signal is noticeable, while at higher temperatures, the HE dominates, with the two effects having opposite signs. Above  $T_c$ , only the HE is present, as  $R_{Antisym}$  tends to 0 at  $B = 0$ . Below this temperature, there is still a contribution from the AHE.

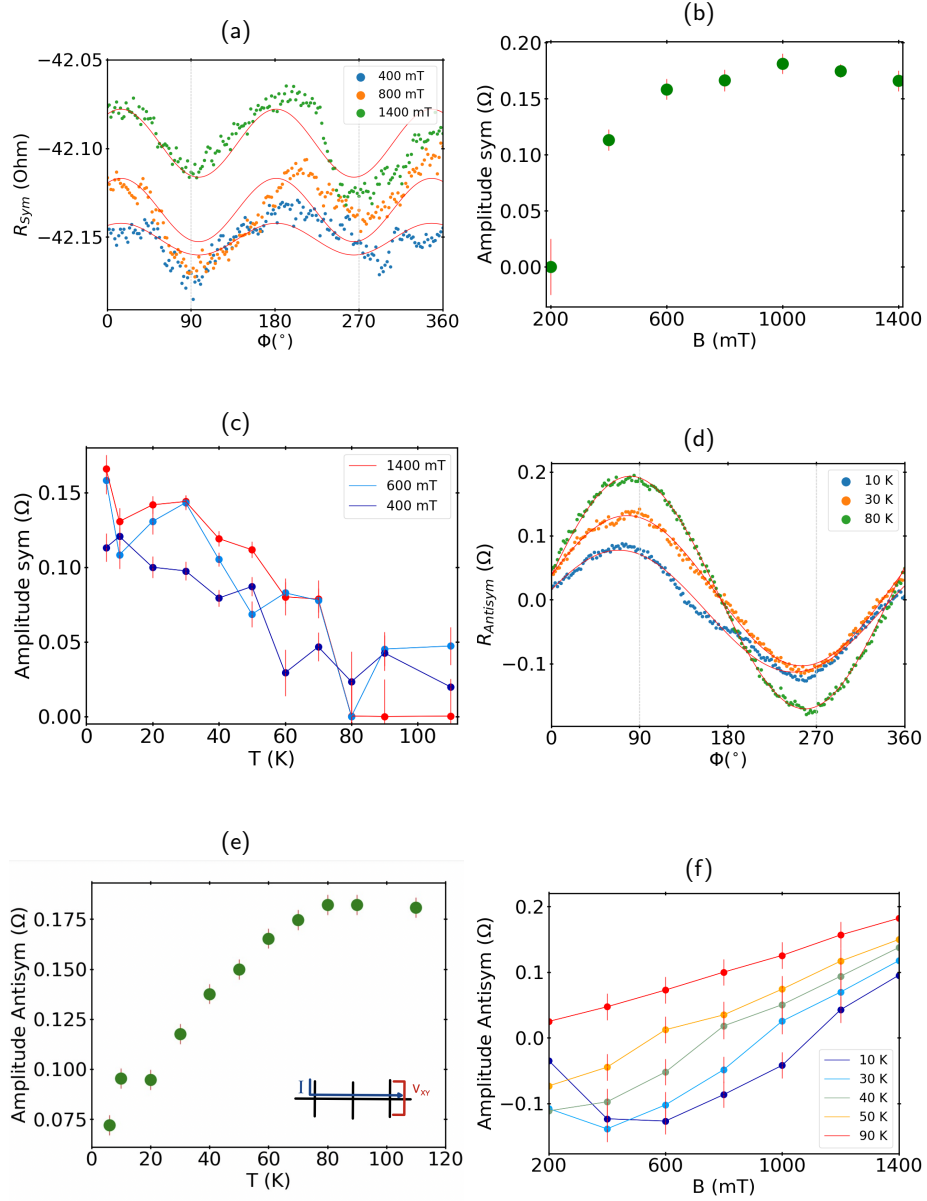


Figure 4.5: a| Symmetric part of the transverse resistance as a function of the in-plane angle of the magnetic field at 10 K for different values of the magnetic field, with the fit given by Eq.4.1. b| Amplitude of the fit from the symmetric part as a function of the magnetic field at 10 K. c| Amplitude of the fit from the symmetric part as a function of temperature at 1400 mT. d| Antisymmetric part of the transverse resistance as a function of the in-plane angle of the magnetic field at 1400 mT for different temperatures, with the fit given by Eq.4.2. e| Amplitude of the fit from the antisymmetric part as a function of temperature at 1400 mT, and a schematic representation of the current flow and voltage measurement in the first axis configuration. f| Amplitude of the fit from the Antisymmetric part as a function of the magnetic field at 10 K. Applied current in the x direction (first axis).

#### 4.4.2 Second axis

For the second axis, where the current flows along the y-axis, a  $90^\circ$  shift was applied to the angle in the symmetric part, in order to align the  $\phi = 0$  with the current direction. Figure 4.6a shows the data for both the first and second axes. The primary aim of this section is to determine whether there is a discernible shift in the data for the symmetric part. This is crucial because, while a shift does not manifest in AMR it could potentially occur in SHMR. As discussed in previous sections, the change in the resistance behavior depending on the current axis could be attributed to SHMR, as the AMR effect in the resistance should remain unchanged when changing the current axis (after the  $90^\circ$  shift when changing the current axis), because it depends only on the angle between the current direction and magnetization, which are the same for both crystallographic axes. The SHMR depends on the SHE and the angle of spin polarization, implying that the observed change in resistance behavior when changing the current axis could be due to this effect.

Upon analyzing the data [Figure 4.6a], it becomes apparent that no shift can be unambiguously determined within the precision of the measurements. The absence of a shift does not conclusively negate the possibility of SHMR, as the orientation of the spin polarization remains undetermined within the current experimental setup. Further studies are necessary to draw definitive conclusions. These should include investigations on other planes, as outlined in the theory section.

For the antisymmetric part, a  $90^\circ$  shift when changing the current axis was unnecessary because the antisymmetric resistance arises from the out-of-plane component of the misaligned magnetic field, which remains the same when the current direction changes. Figure 4.6b shows the antisymmetric part of the resistance with current applied through both the first and second axes, demonstrating no shift in the position of the extrema.

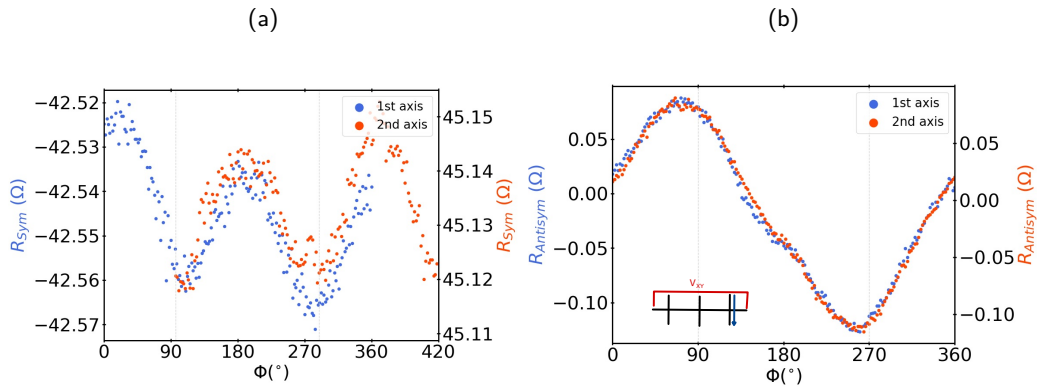


Figure 4.6: a| Symmetric part of the transverse resistance as a function of the in-plane angle of the magnetic field, at  $B=1400$  mT and  $T=10$  K. In blue, the current is applied along the x-axis (first axis), and in orange, the current is applied along the y-axis (second axis). b| Antisymmetric part of the transverse resistance as a function of the in-plane angle of the magnetic field. In blue, the current is applied along the x-axis (first axis), and in orange, the current is applied along the y-axis (second axis), and a schematic representation of the current flow and voltage measurement in the second axis configuration.

## 5 Conclusions and outlook

This thesis aimed to explore magnetic proximity effects in vdW heterostructures, specifically focusing on bilayers composed of  $\text{WTe}_2$  and CGT. The research findings indicate that annealing at least  $T=280^\circ\text{C}$  for 3 hours, plays a crucial role in observing AHE signals in  $\text{WTe}_2$ , enhancing the quality of the vdW interface with CGT; thicker CGT layers appear to require higher annealing temperatures (at  $T=330^\circ\text{C}$ ). Remarkably, the temperature dependence of longitudinal and transverse resistances revealed a critical temperature that is significantly larger than the parent CGT, with an average of 96.5 K across the devices exhibiting an AHE signal (4 out of 6 devices). This represents a 53% increase from the  $T_c$  of 63 K of pristine CGT. A possible explanation for this increase in  $T_c$  is the SOC of  $\text{WTe}_2$  stabilizing the ferromagnetic order in CGT. Such an effect should be confined to a thin region at the interface. An alternative explanation is that annealing affects the CGT, increasing the  $T_C$  of the bulk.

While the observation of the AHE- and AMR-like signals could be ascribed to magnetic proximity effects, there exist other phenomena, unrelated to proximity effects like SHMR, that can lead to similar results. The analysis of the symmetric components of transverse resistance as a function of the in-plane angle of the magnetic field, which exhibits a  $\cos^2$  dependency, can be used to discriminate between the different origins. For example, a shift in the minima, when the current is measured along different axes, would favor the interpretation by SHMR. However, such a shift could not be unambiguously established in our preliminary measurements. To conclusively attribute our observations to either proximity effects or SHMR, further investigations are needed, particularly involving angular dependence measurements on different planes.

Looking ahead, the long-term objective of this research is to reduce the thickness of  $\text{WTe}_2$  to a monolayer, where it becomes a topological insulator. The goal is to induce magnetism through proximity effects and measure the QAHE. In this limit, the SHMR should be zero, thus the simple observation of AHE or AMR would likely be sufficient to establish the presence of proximity magnetism. Achieving this goal would provide significant insights into the behavior of topological insulators and open new possibilities for developing advanced quantum devices with tailored magnetic properties.

In summary, while the initial goal of observing magnetic proximity effects was partially achieved, the potential presence of SHMR necessitates further research. This thesis lays a foundational understanding of the interactions within  $\text{WTe}_2/\text{CGT}$  heterostructures and outlines a clear path for future studies to distinguish between proximity effects and SHMR. Ultimately, this research advances the field of spintronics, providing a basis for the development of novel topological devices..

## Bibliography

- [AAF<sup>+</sup>21] Rajdeep Adhikari, Soma Adhikari, Bogdan Faina, Marc Terschanski, Sophie Bork, Claudia Leimhofer, Mirko Cinchetti, and Alberta Bonanni. Positive magnetoresistance and chiral anomaly in exfoliated type-ii weyl semimetal td-WTe<sub>2</sub>. *Nanomaterials*, 11:2755, 10 2021.
- [AXF<sup>+</sup>14] Mazhar N. Ali, Jun Xiong, Steven Flynn, Jing Tao, Quinn D. Gibson, Leslie M. Schoop, Tian Liang, Neel Haldolaarachchige, Max Hirschberger, N. P. Ong, and R. J. Cava. Large, non-saturating magnetoresistance in WTe<sub>2</sub>. *Nature*, 514(7521):205–208, 2014.
- [BAG<sup>+</sup>20] Semonti Bhattacharyya, Golrokh Akhgar, Matt Gebert, Julie Karel, Mark Edmonds, and Michael Fuhrer. Recent progress in proximity coupling of magnetism to topological insulators, 12 2020.
- [BAG<sup>+</sup>21] Semonti Bhattacharyya, Golrokh Akhgar, Matthew Gebert, Julie Karel, Mark T. Edmonds, and Michael S. Fuhrer. Recent progress in proximity coupling of magnetism to topological insulators. *Advanced Materials*, 33(33):2007795, 2021.
- [Ber70] L. Berger. Side-jump mechanism for the hall effect of ferromagnets. *Phys. Rev. B*, 2:4559–4566, Dec 1970.
- [BGR16] G.R. Bhimanapati, N.R. Glavin, and J.A. Robinson. Chapter three - 2d boron nitride: Synthesis and applications. In Francesca Iacopi, John J. Boeckl, and Chennupati Jagadish, editors, *2D Materials*, volume 95 of *Semiconductors and Semimetals*, pages 101–147. Elsevier, 2016.
- [BSS85] H.P. Boehm, R. Setton, and E. Stumpp. Nomenclature and terminology of graphite intercalation compounds. report by a subgroup of the international committee for characterization and terminology of carbon and graphite on suggestions for rules for the nomenclature and terminology of graphite intercalation compounds. *Synthetic Metals*, 11(6):363–371, 1985.
- [BSST<sup>+</sup>17] L. Antonio Benítez, Juan F. Sierra, Williams Savero Torres, Aloïs Arrighi, Frédéric Bonell, Marius V. Costache, and Sergio O. Valenzuela. Strongly anisotropic spin relaxation in graphene–transition metal dichalcogenide heterostructures at room temperature. *Nature Physics*, 14(3):303–308, December 2017.
- [CBOA95] V. Carteaux, Dominique Brunet, Guy Ouvrard, and Gilles André. Crystallographic, magnetic and electronic structures of a new layered ferromagnetic compound cr<sub>2</sub>ge<sub>2</sub>te<sub>6</sub>. *Journal of Physics: Condensed Matter*, 7:69–87, 1995.
- [CTN<sup>+</sup>13] Yan-Ting Chen, Saburo Takahashi, Hiroyasu Nakayama, Matthias Althammer, Sebastian T. B. Goennenwein, Eiji Saitoh, and Gerrit E. W. Bauer. Theory of spin hall magnetoresistance. *Phys. Rev. B*, 87:144411, Apr 2013.
- [CZF<sup>+</sup>13] Cui-Zu Chang, Jinsong Zhang, Xiao Feng, Jie Shen, Zuocheng Zhang, Minghua Guo, Yunbo Ou, Pang Wei, li Jun, Zhongqing Ji, Yang Feng, Shuaihua Ji, Xi Chen, Jinfeng Jia, Xi Dai, Zhong Fang, Shou-Cheng Zhang, Ke He, and Qi-Kun Xue. Experimental observation of the quantum anomalous hall effect in a magnetic topological insulator. *Science (New York, N.Y.)*, 340, 03 2013.
- [DB20] Antonio Di Bartolomeo. Emerging 2d materials and their van der waals heterostructures. *Nanomaterials*, 10:579, 03 2020.
- [DBPL<sup>+</sup>19] Antonio Di Bartolomeo, Aniello Pelella, Xiaowei Liu, Feng Miao, Maurizio Pasacantando, Filippo Giubileo, Alessandro Grillo, Laura Iemmo, Francesca Urban, and Shi-Jun Liang. Pressure-tunable ambipolar conduction and hysteresis in thin palladium diselenide field effect transistors. *Advanced Functional Materials*, 29(29), May 2019.

- [DYS<sup>+</sup>20] Yujun Deng, Yijun Yu, Meng Zhu Shi, Zhongxun Guo, Zihan Xu, Jing Wang, Xian Hui Chen, and Yuanbo Zhang. Quantum anomalous hall effect in intrinsic magnetic topological insulator  $\text{MnBi}_2\text{Te}_4$ . *Science*, 367(6480):895–900, February 2020.
- [Eft17] Ali Eftekhari. Tungsten dichalcogenides ( $\text{WS}_2$ ,  $\text{WSe}_2$ , and  $\text{WTe}_2$ ): Materials chemistry and applications. *J. Mater. Chem. A*, 5, 07 2017.
- [FWC<sup>+</sup>18] Valla Fatemi, Sanfeng Wu, Yuan Cao, Landry Bretheau, Quinn D. Gibson, Kenji Watanabe, Takashi Taniguchi, Robert J. Cava, and Pablo Jarillo-Herrero. Electrically tunable low-density superconductivity in a monolayer topological insulator. *Science*, 362(6417):926–929, November 2018.
- [FZP<sup>+</sup>18] Zaiyao Fei, Wenjin Zhao, Tauno A. Palomaki, Bosong Sun, Moira K. Miller, Zhiying Zhao, Jiaqiang Yan, Xiaodong Xu, and David H. Cobden. Ferroelectric switching of a two-dimensional metal, 2018.
- [GF15] Martin Gmitra and Jaroslav Fabian. Graphene on transition-metal dichalcogenides: A platform for proximity spin-orbit physics and optospintronics. *Physical Review B*, 92(15), October 2015.
- [GG13] A. K. Geim and I. V. Grigorieva. Van der waals heterostructures. *Nature*, 499(7459):419–425, July 2013.
- [GIAKvW17] Talieh S Ghiasi, Josep Ingla-Aynés, Alexey A Kaverzin, and Bart J van Wees. Large proximity-induced spin lifetime anisotropy in transition-metal dichalcogenide/graphene heterostructures. *Nano letters*, 17(12):7528–7532, December 2017.
- [GKD<sup>+</sup>21] Talieh S. Ghiasi, Alexey A. Kaverzin, Avalon H. Dismukes, Dennis K. de Wal, Xavier Roy, and Bart J. van Wees. Electrical and thermal generation of spin currents by magnetic bilayer graphene. *Nature Nanotechnology*, 16(7):788–794, May 2021.
- [GLL<sup>+</sup>17a] Cheng Gong, Lin Li, Zhenglu Li, Huiwen Ji, Alex Stern, Yang Xia, Ting Cao, Wei Bao, Chenzhe Wang, Yuan Wang, Z. Q. Qiu, R. J. Cava, Steven G. Louie, Jing Xia, and Xiang Zhang. Discovery of intrinsic ferromagnetism in two-dimensional van der waals crystals. *Nature*, 546(7657):265–269, April 2017.
- [GLL<sup>+</sup>17b] Cheng Gong, Lin Li, Zhenglu Li, Huiwen Ji, Alex Stern, Yang Xia, Ting Cao, Wei Bao, Chenzhe Wang, Yuan Wang, Z. Q. Qiu, R. J. Cava, Steven G. Louie, Jing Xia, and Xiang Zhang. Discovery of intrinsic ferromagnetism in two-dimensional van der waals crystals. *Nature*, 546(7657):265–269, 2017.
- [GLQ<sup>+</sup>18] Enlai Gao, Shao-Zhen Lin, Zhao Qin, Markus Buehler, and Zhiping Xu. Mechanical exfoliation of two-dimensional materials. *Journal of the Mechanics and Physics of Solids*, 115, 03 2018.
- [Hal80] E.H. Hall. Xxxviii. on the new action of magnetism on a permanent electric current. *The London, Edinburgh, and Dublin Philosophical Magazine and Journal of Science*, 10(63):301–328, 1880.
- [Hal81] E.H. Hall. Xviii. on the “rotational coefficient” in nickel and cobalt. *The London, Edinburgh, and Dublin Philosophical Magazine and Journal of Science*, 12(74):157–172, 1881.
- [HDK<sup>+</sup>18] Gang Hee Han, Dinh Loc Duong, Dong Hoon Keum, Seok Joon Yun, and Young Hee Lee. van der waals metallic transition metal dichalcogenides. *Chemical Reviews*, 118(13):6297–6336, 07 2018.
- [JNM02] T. Jungwirth, Qian Niu, and A. H. MacDonald. Anomalous hall effect in ferromagnetic semiconductors. *Phys. Rev. Lett.*, 88:207208, May 2002.



- [Jou19] Magnetic 2d materials and heterostructures. *Nature Nanotechnology*, 14(5):408–419, 2019.
- [KTO<sup>+</sup>24] I-Hsuan Kao, Junyu Tang, Gabriel Calderon Ortiz, Menglin Zhu, Sean Yuan, Rahul Rao, Jiahua Li, James H. Edgar, Jiaqiang Yan, David G. Mandrus, Kenji Watanabe, Takashi Taniguchi, Jinwoo Hwang, Ran Cheng, Jyoti Katoch, and Simranjeet Singh. Unconventional unidirectional magnetoresistance in vdW heterostructures, 2024.
- [LGMS<sup>+</sup>20] T. P. Lyons, D. Gillard, A. Molina-Sánchez, A. Misra, F. Withers, P. S. Keatley, A. Kozikov, T. Taniguchi, K. Watanabe, K. S. Novoselov, J. Fernández-Rossier, and A. I. Tartakovsky. Interplay between spin proximity effect and charge-dependent exciton dynamics in  $\text{MoSe}_2/\text{CrBr}_3$  van der Waals heterostructures. *Nature Communications*, 11(1):6021, 2020.
- [LGZ<sup>+</sup>13] Zheng Liu, Yongji Gong, Wu Zhou, Lulu Ma, Jingjiang Yu, Juan Carlos Idrobo, Jeil Jung, Allan H. MacDonald, Robert Vajtai, Jun Lou, and Pulickel M. Ajayan. Ultrathin high-temperature oxidation-resistant coatings of hexagonal boron nitride. *Nature Communications*, 4(1):2541, 2013.
- [LHW<sup>+</sup>17] Xiao-Li Li, Wen Han, Jiangbin Wu, Xiao-Fen Qiao, Jun Zhang, and Ping-Heng Tan. Layer-number dependent optical properties of 2d materials and their application for thickness determination. *Advanced Functional Materials*, 27:1604468, 05 2017.
- [LRL<sup>+</sup>22] Junxue Li, Mina Rashetnia, Mark Lohmann, Jahyun Koo, Youming Xu, Xiao Zhang, Kenji Watanabe, Takashi Taniguchi, Shuang Jia, Xi Chen, Binghai Yan, Yong-Tao Cui, and Jing Shi. Proximity-magnetized quantum spin hall insulator: monolayer  $1\text{t}'\text{WTe}_2/\text{Cr}_2\text{Ge}_2\text{Te}_6$ . *Nature Communications*, 13(1):5134, 2022.
- [LSN<sup>+</sup>19] Mark Lohmann, Tang Su, Ben Niu, Yusheng Hou, Mohammed Alghamdi, Mohammed Aldosary, Wenyu Xing, Jiangnan Zhong, Shuang Jia, Wei Han, Ruqian Wu, Yong-Tao Cui, and Jing Shi. Probing magnetism in insulating  $\text{Cr}_2\text{Ge}_2\text{Te}_6$  by induced anomalous hall effect in  $\text{Pt}$ . *Nano Letters*, 19(4):2397–2403, March 2019.
- [LTAS14] Tao Lin, Chi Tang, Hamad M. Alyahyaei, and Jing Shi. Experimental investigation of the nature of the magnetoresistance effects in  $\text{Pd-Yig}$  hybrid structures. *Phys. Rev. Lett.*, 113:037203, Jul 2014.
- [LWH<sup>+</sup>17] Peng Li, Yan Wen, Xin He, Qiang Zhang, Chuan Xia, Zhi-Ming Yu, Shengyuan A. Yang, Zhiyong Zhu, Husam N. Alshareef, and Xi-Xiang Zhang. Evidence for topological type-II Weyl semimetal  $\text{WTe}_2$ . *Nature Communications*, 8(1):2150, 2017.
- [LZQ15] Chao-Xing Liu, Shou-Cheng Zhang, and Xiao-Liang Qi. The quantum anomalous hall effect, 2015.
- [MLH<sup>+</sup>10] Kin Fai Mak, Changgu Lee, James Hone, Jie Shan, and Tony F. Heinz. Atomically thin  $\text{MoS}_2$ : A new direct-gap semiconductor. *Phys. Rev. Lett.*, 105:136805, Sep 2010.
- [MOP<sup>+</sup>17] Sajede Manzeli, Dmitry Ovchinnikov, Diego Pasquier, Oleg V. Yazyev, and Andras Kis. 2D transition metal dichalcogenides. *Nature Reviews Materials*, 2(8):17033, August 2017.
- [NAC<sup>+</sup>13] H. Nakayama, M. Althammer, Y.-T. Chen, K. Uchida, Y. Kajiwara, D. Kikuchi, T. Ohtani, S. Geprägs, M. Opel, S. Takahashi, R. Gross, G. E. W. Bauer, S. T. B. Goennenwein, and E. Saitoh. Spin hall magnetoresistance induced by a nonequilibrium proximity effect. *Physical Review Letters*, 110(20), May 2013.
- [NGM<sup>+</sup>04] K. S. Novoselov, A. K. Geim, S. V. Morozov, D. Jiang, Y. Zhang, S. V. Dubonos,

- I. V. Grigorieva, and A. A. Firsov. Electric field effect in atomically thin carbon films. *Science*, 306(5696):666–669, 2004.
- [NMCN16] K. S. Novoselov, A. Mishchenko, A. Carvalho, and A. H. Castro Neto. 2d materials and van der waals heterostructures. *Science*, 353(6298):aac9439, 2016.
- [OSN06] Shigeki Onoda, Naoyuki Sugimoto, and Naoto Nagaosa. Intrinsic versus extrinsic anomalous hall effect in ferromagnets. *Phys. Rev. Lett.*, 97:126602, Sep 2006.
- [PGJ<sup>+</sup>16] Filippo Pizzocchero, Lene Gammelgaard, Bjarke S. Jessen, José M. Caridad, Lei Wang, James Hone, Peter Bøggild, and Timothy J. Booth. The hot pick-up technique for batch assembly of van der waals heterostructures. *Nature Communications*, 7(1), June 2016.
- [PLK<sup>+</sup>23] Darius Pohl, Yejin Lee, Dominik Kriegner, Sebastian Beckert, Sebastian Schneider, Bernd Rellinghaus, and Andy Thomas. Probing magnetic properties at the nanoscale: in-situ hall measurements in a tem. *Scientific Reports*, 13(1):14871, 2023.
- [Pug30] Emerson M. Pugh. Hall effect and the magnetic properties of some ferromagnetic materials. *Phys. Rev.*, 36:1503–1511, Nov 1930.
- [QLFL14] Xiaofeng Qian, Junwei Liu, Liang Fu, and Ju Li. Quantum spin hall effect in two-dimensional transition metal dichalcogenides. *Science*, 346(6215):1344–1347, 2014.
- [SFK<sup>+</sup>21] Juan F. Sierra, Jaroslav Fabian, Roland K. Kawakami, Stephan Roche, and Sergio O. Valenzuela. Van der waals heterostructures for spintronics and opto-spintronics. *Nature Nanotechnology*, 16(8):856–868, July 2021.
- [Smi58] J. Smit. The spontaneous hall effect in ferromagnetics ii. *Physica*, 24(1):39–51, 1958.
- [SPW<sup>+</sup>16] Qingjun Song, Xingchen Pan, Haifeng Wang, Kun Zhang, Qinghai Tan, Pan Li, Yi Wan, Yilun Wang, Xiaolong Xu, Miaoling Lin, Xiangang Wan, Fengqi Song, and Lun Dai. The in-plane anisotropy of WTe<sub>2</sub> investigated by angle-dependent and polarized raman spectroscopy. *Scientific Reports*, 6(1):29254, 2016.
- [THP<sup>+</sup>23] Joachim Dahl Thomsen, Myung-Geun Han, Aubrey Penn, Alexandre C. Foucher, Michael Geiwitz, Kenneth S. Burch, Lukáš Děkanovský, Zdeněk Sofer, Yu Liu, Cedimir Petrovic, Frances M. Ross, Yimei Zhu, and Prineha Narang. Magnetic property control of cr<sub>2</sub>ge<sub>2</sub>te<sub>6</sub> through oxidation and thickness effects, 2023.
- [WWL<sup>+</sup>19] Yaojia Wang, Lizheng Wang, Xiaowei Liu, Heng Wu, Pengfei Wang, Dayu Yan, Bin Cheng, Youguo Shi, Kenji Watanabe, Takashi Taniguchi, Shi-Jun Liang, and Feng Miao. Direct evidence for charge compensation-induced large magnetoresistance in thin WTe<sub>2</sub>. *Nano Letters*, 19(6):3969–3975, 06 2019.
- [WYH<sup>+</sup>15a] Hongming Weng, Rui Yu, Xiao Hu, Xi Dai, and Zhong Fang. Quantum anomalous hall effect and related topological electronic states. *Advances in Physics*, 64(3):227–282, May 2015.
- [WYH<sup>+</sup>15b] Hongming Weng, Rui Yu, Xiao Hu, Xi Dai, and Zhong Fang. Quantum anomalous hall effect and related topological electronic states. *Advances in Physics*, 64(3):227–282, May 2015.
- [XCN10] Di Xiao, Ming-Che Chang, and Qian Niu. Berry phase effects on electronic properties. *Rev. Mod. Phys.*, 82:1959–2007, Jul 2010.
- [XCO<sup>+</sup>17] Wenyu Xing, Yangyang Chen, Patrick M Odenthal, Xiao Zhang, Wei Yuan, Tang Su, Qi Song, Tianyu Wang, Jiangnan Zhong, Shuang Jia, X C Xie, Yan Li, and Wei Han. Electric field effect in multilayer cr<sub>2</sub>ge<sub>2</sub>te<sub>6</sub>: a ferromagnetic 2d material. *2D Materials*, 4(2):024009, May 2017.

- [YKM<sup>+</sup>04] Yugui Yao, Leonard Kleinman, A. H. MacDonald, Jairo Sinova, T. Jungwirth, Ding-sheng Wang, Enge Wang, and Qian Niu. First principles calculation of anomalous hall conductivity in ferromagnetic bcc fe. *Phys. Rev. Lett.*, 92:037204, Jan 2004.
- [YLW<sup>+</sup>18] Yumeng Yang, Ziyang Luo, Haijun Wu, Yanjun Xu, Run-Wei Li, Stephen Pennycook, Shufeng Zhang, and Yihong Wu. Anomalous hall magnetoresistance in a ferromagnet. *Nature Communications*, 9, 06 2018.
- [YVC<sup>+</sup>22] Hyunsoo Yang, Sergio O. Valenzuela, Mairbek Chshiev, Sébastien Couet, Bernard Dieny, Bruno Dlubak, Albert Fert, Kevin Garello, Matthieu Jamet, Dae-Eun Jeong, Kangho Lee, Taeyoung Lee, Marie-Blandine Martin, Gouri Sankar Kar, Pierre Sénéor, Hyeon-Jin Shin, and Stephan Roche. Two-dimensional materials prospects for non-volatile spintronic memories. *Nature*, 606(7915):663–673, 2022.
- [ZKW<sup>+</sup>21] Xurui Zhang, Vivek Kakani, John M. Woods, Judy J. Cha, and Xiaoyan Shi. Thickness dependence of magnetotransport properties of tungsten ditelluride. *Phys. Rev. B*, 104:165126, Oct 2021.
- [ZKZ<sup>+</sup>20] Bing Zhao, Dmitrii Khokhriakov, Yang Zhang, Huixia Fu, Bogdan Karpiak, Anamul Md. Hoque, Xiaoguang Xu, Yong Jiang, Binghai Yan, and Saroj P. Dash. Observation of charge to spin conversion in weyl semimetal WTe<sub>2</sub> at room temperature. *Physical Review Research*, 2(1), March 2020.
- [ZMAS<sup>+</sup>18] Igor Zutic, Alex Matos-Abiad, Benedikt Scharf, Hanan Dery, and Kirill Belashchenko. Proximitized materials, 2018.
- [ZSL<sup>+</sup>20] Ding Zhong, Kyle L. Seyler, Xiayu Linpeng, Nathan P. Wilson, Takashi Taniguchi, Kenji Watanabe, Michael A. McGuire, Kai-Mei C. Fu, Di Xiao, Wang Yao, and Xiaodong Xu. Layer-resolved magnetic proximity effect in van der waals heterostructures. *Nature Nanotechnology*, 15(3):187–191, January 2020.
- [ZZS<sup>+</sup>16] Xiao Zhang, Yuele Zhao, Qi Song, Shuang Jia, Jing Shi, and Wei Han. Magnetic anisotropy of the single-crystalline ferromagnetic insulator Cr<sub>2</sub>Ge<sub>2</sub>Te<sub>6</sub>. *Japanese Journal of Applied Physics*, 55(3):033001, February 2016.

## A Differentiating magnetic proximity effect and spin Hall magnetoresistance effect in a low-symmetry crystal

Following the description of the differentiating process for a high symmetry crystal, the schematic illustration for the three cases, the high symmetry case, the low symmetry case with the current flowing in the  $x$ -axis, considering that this one is the first crystallographic axis of the crystal, and the low symmetry case with the current flowing in the  $y$ -axis, considering that this one is the second crystallographic axis of the crystal, is shown here.

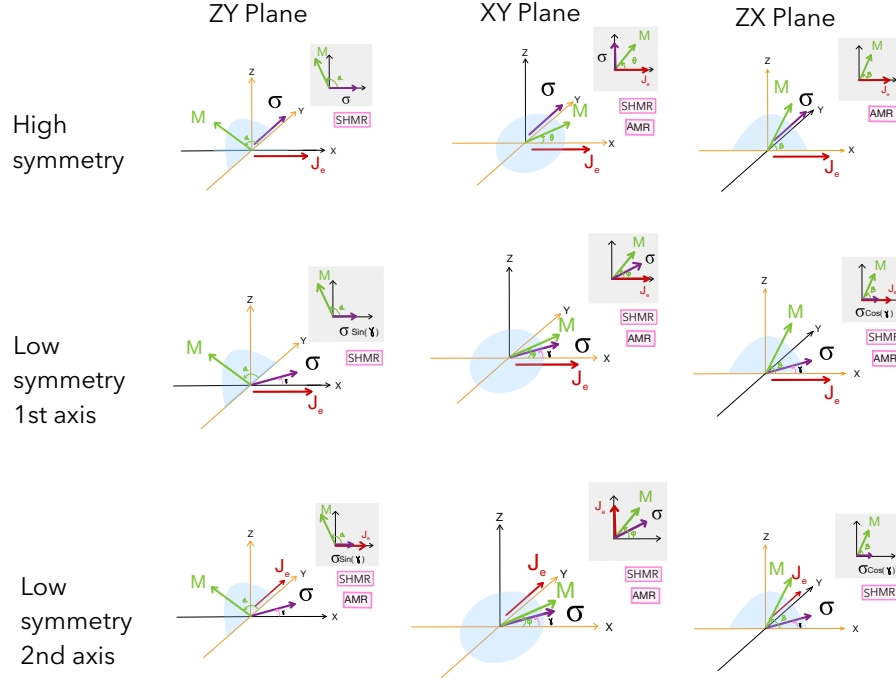


Figure A.1: Illustration of geometric relation between the the charge current ( $J_e$ ), the spin polarization ( $\sigma$ ), and magnetization ( $M$ ), in the case three cases: high symmetry crystal, low symetry crystal with the current flowing in the first crystallographic axis, and in the second. In pink is highlighted the phenomenon, spin Hall magnetoresistance (SHMR) or anisotropic magnetoresistance (AMR), that can take place by the rotation of  $M$  in each plane.

## B Gate dependence

One of the measurements carried out on the devices has been the gate dependence of the charge carrier density. The effect of the gate voltage on energy levels is significant: in metals (or semimetals, as  $\text{WTe}_2$ ), that have overlapping energy bands with a partially filled conduction band and a partially filled valence band, the Fermi energy resides within the conduction band, allowing a high density of free charge carriers (electrons). While in semiconductors (as CGT) at absolute zero, the Fermi energy lies in the middle of the band gap. By gate voltage applied between the doped substrate of silicon that is located under the  $\text{SiO}_2$  (through a scratch on the substrate) and the Pd contact that is connected to the ground. With this configuration a vertical electric field is generated where the dielectric is the  $\text{SiO}_2$  layer on the substrate and the capacitor plates are doped Si and the Pd contact on the sample. This allows varying the Fermi level of each material, thereby modifying the charge carrier density in both  $\text{WTe}_2$  and CGT. However, if CGT has a large band gap and is insulating, this will remain so, and the variation will be due to changes in the charge carrier density in  $\text{WTe}_2$ .

Following the 4.3 section, the analysis will be based on the measurements obtained from device 5.

The electric transport properties of the  $\text{WTe}_2$  layer can be controlled by applying an electrostatic gate voltage, which adjusts the Fermi energy of the material. Figure B.1d illustrates the longitudinal resistance ( $R_{xx}$ ) as a function of the gate voltage at a base temperature of 6 K. Here,  $R_{xx}$  increases with higher gate voltages, suggesting that  $\text{WTe}_2$  is likely hole-doped. Owing to, a positive gate voltage attracts electrons and repels holes. Consequently, for electron-doped materials, increasing the voltage facilitates easier electron movement, thereby reducing resistance. Conversely, in hole-doped materials, applying a positive voltage repels holes, leading to increased resistance as the voltage rises.

Figure B.1a depicts the transverse resistance ( $R_{xy}$ ) as a function of the out-of-plane magnetic field for device 5 at various gate voltages. Similar to the temperature dependence discussed earlier, the saturation in  $R_{xy}$  [Figure B.1c] occurs at higher magnetic fields compared to pristine CGT, where magnetization saturation occurs around  $B_z = 50$  mT with negligible coercivity [KTO+24].

Following the analysis from the previous section, from the slope of the linear fit of Figure B.1c, one can extract the charge carrier density ( $n$ ) as a function of gate voltage, shown in Figure B.1b. It is easy to see, that the magnitude of  $n$  is suppressed (enhanced) by positive (negative) gate voltages, in agreement with the above discussion of the gate dependence of  $R_{xx}$ .

This part involves a subtlety, which is the sign convention. The consensus that considers the direction of the magnetic field, which in this case points towards the sample, and the direction of the current as indicated in figure B.1b has been followed. With this information, the transverse accumulation of charges is determined using the Lorentz law ( $\vec{F} = q(\vec{v} \times \vec{B})$ ), to ascertain if the voltage contacts are in the correct order with the aim of assign the sign of carrier density.

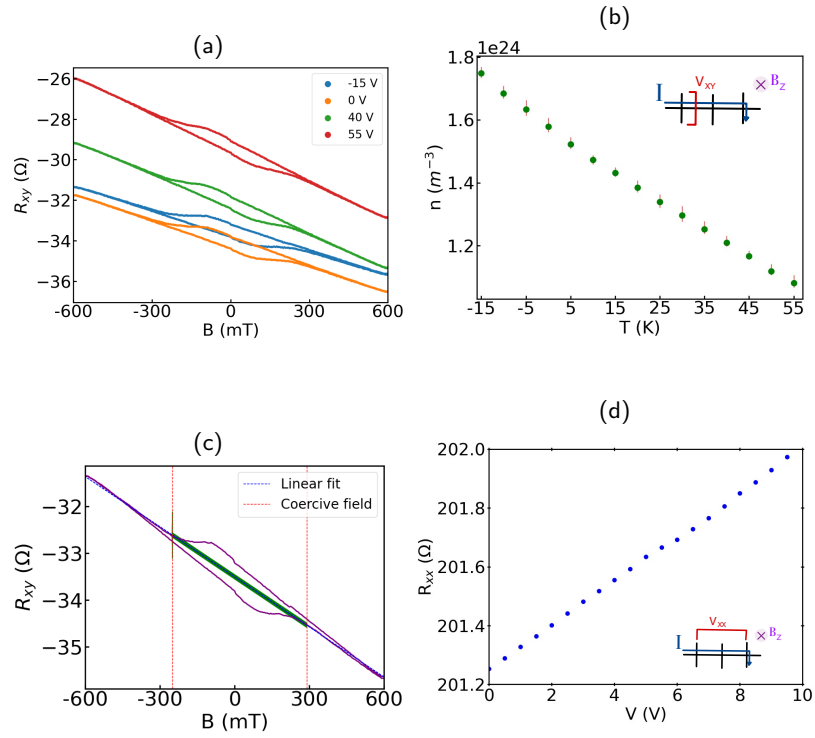
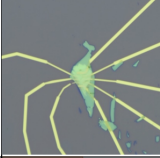
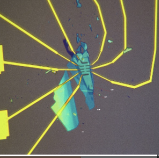
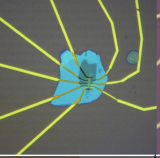
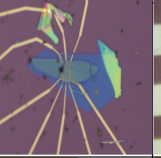
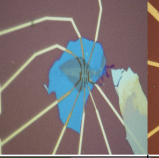
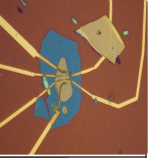


Figure B.1: a| Transverse resistance ( $R_{xy}$ ) as a function of out-of-plane magnetic field ( $B_z$ ) for different gate voltages ( $V$ ). b|  $R_{xy}$  as a function of  $B_z$  for  $T=6$  K and  $V= -15$  V. Blue dashed line corresponds to the linear fit, red dashed line marks where the hysteresis loop closes, and green indicates the width of the hysteresis loop. c| charge carrier density for different voltages. d| Longitudinal resistance ( $R_{xx}$ ) as a function of gate voltage. In c| and d| there is a scheme of the contact design.

## C Further details on the device overview

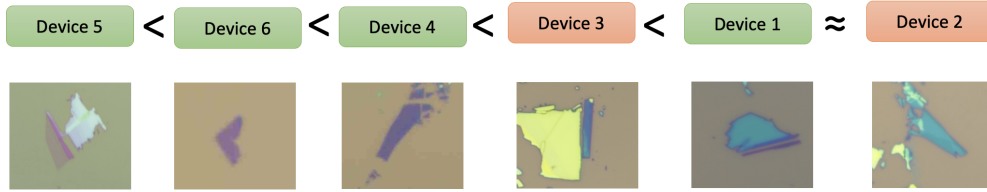
In this appendix section, more detailed Figures are provided for those presented in Section 4.1. Specifically, images of the flakes will be shown to give an idea of the materials that comprised the heterostructure of each device.

	Device 1	Device 2	Device 3	Device 4	Device 5	Device 6
						
Annealing Temperatures	220°C	220°C	220°C	220°C	280°C	280°C
	280°C	280°C	280°C	280°C		330°C
			330°C			

No AHE
  AHE

Figure C.1: Overview of fabricated and measured devices in chronological order with annealing temperatures. Red indicates temperatures where AHE was not observed, while green indicates where it was observed.

$\text{WTe}_2$



CGT:

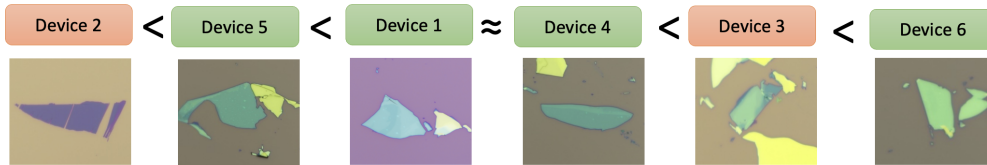


Figure C.2: Measured devices arranged in order of thickness, for  $\text{WTe}_2$  and CGT, from thinnest to thickest. Devices exhibiting anomalous Hall signal are highlighted in green, while those without AHE signal are highlighted in red.

## D Complementary temperature dependence of the longitudinal resistance

In this section, the longitudinal resistance is shown as a function of temperature for the metallic part of device 5, which corresponds to the side where all results in the study have been presented.

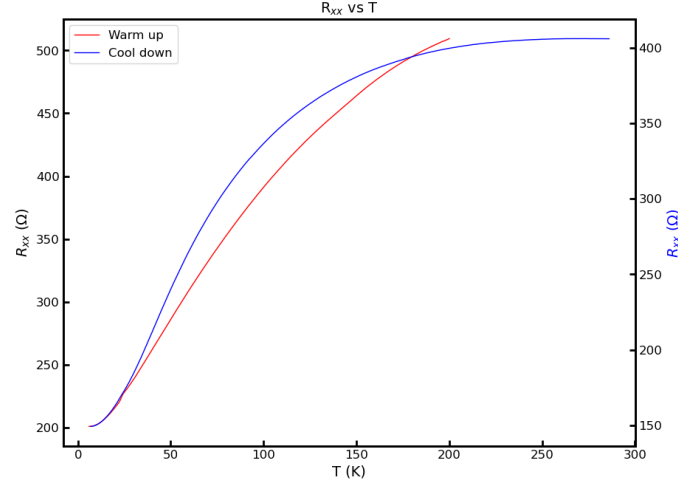


Figure D.1: Temperature dependence of  $R_{xx}$  after the annealing at  $|T_{\text{an}}| = 280^\circ$  of the device 5. In blue the cool down measurements and in red the warm up.



## E Complementary magneto-transport measurements

In this section, the transverse resistance is shown as a function of temperature and out-of-plane magnetic field for device 5 and device 1. For device 5, the individual dependence of transverse resistance on out-of-plane magnetic field is additionally included, highlighting specific temperatures to observe the attenuation of the AHE signal with increasing temperature.

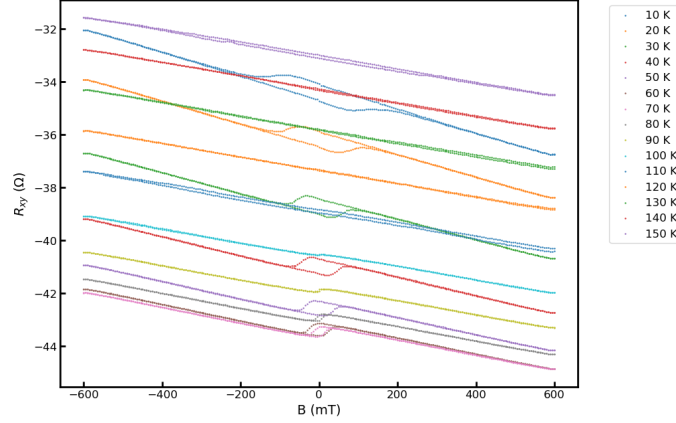


Figure E.1: Temperature dependence of  $R_{xy}$  as a function of the magnetic field out-of-plane, for the device 5.

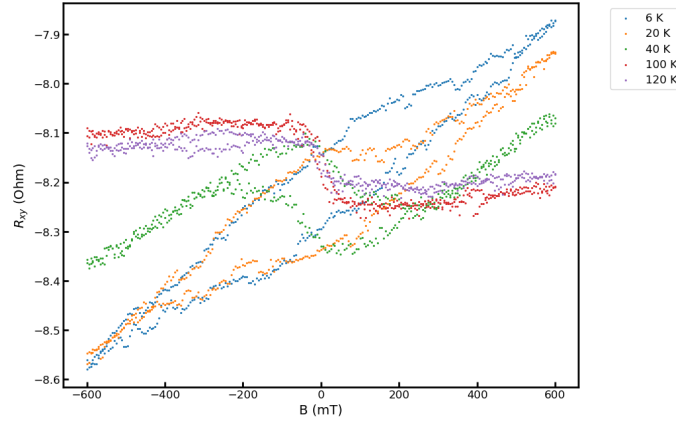


Figure E.2: Temperature dependence of  $R_{xy}$  as a function of the magnetic field out-of-plane, for the device 1.

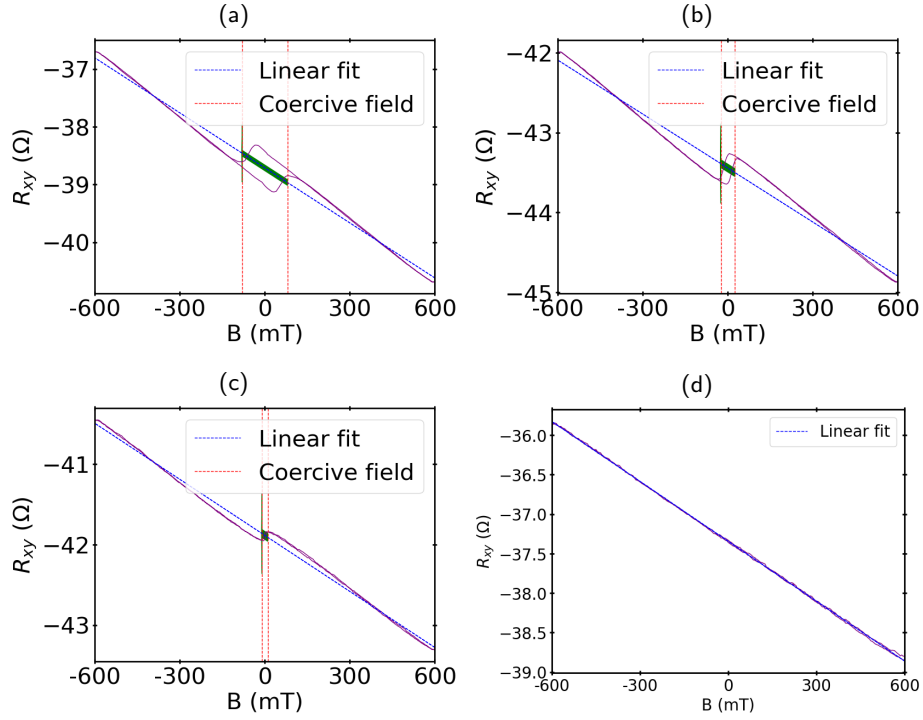


Figure E.3:  $R_{xy}$  as a function of the out-of-plane magnetic field for a)  $T=30$  K,  $T=70$  K,  $T=90$  K,  $T=120$  K. with a linear fit, and in red the coercive field. For device 5

## F Complementary angle dependence for the in-plane magnetic field

This section presents the transverse resistance of device 5 as a function of the angle of the in-plane magnetic field, for different values of magnetic field strength and temperature. First, the symmetric part is shown, followed by the antisymmetric part, which exhibits a sign change for magnetic field values greater than 600 mT. This corresponds to the saturation field, where, beyond this field value and for temperatures above the critical temperature found in previous sections, the HE predominates over the AHE.

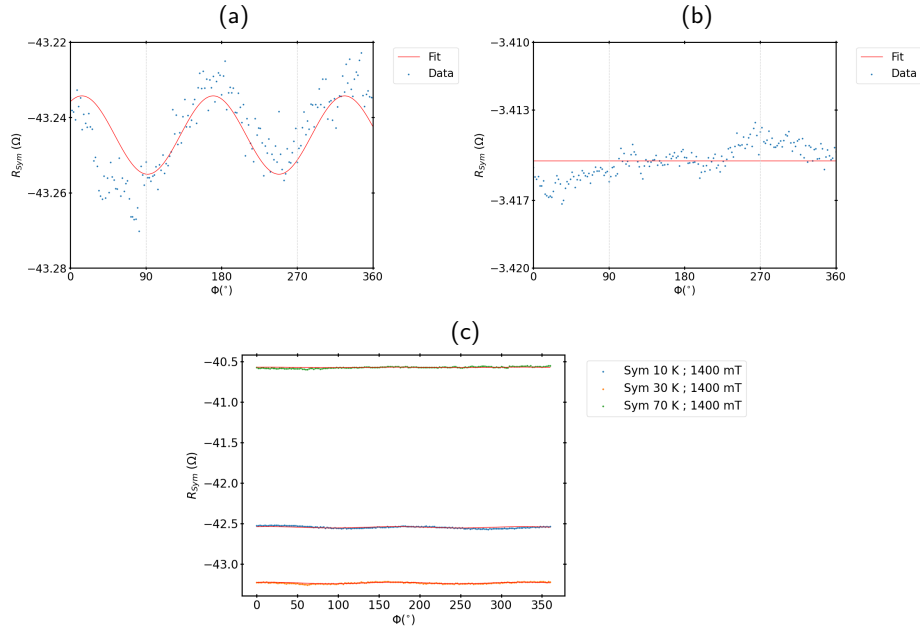


Figure F.1: Symmetric part of  $R_{xy}$  as a function of the angle of the in-plane magnetic field for a)  $T=30$  K and  $B=1000$  mT, b)  $T=110$  K and  $B=1000$  mT, with their fits, respectively. c)  $B=1400$ , and different values of the temperature ( $T=10$  K,  $T=30$  K,  $T=70$  K)

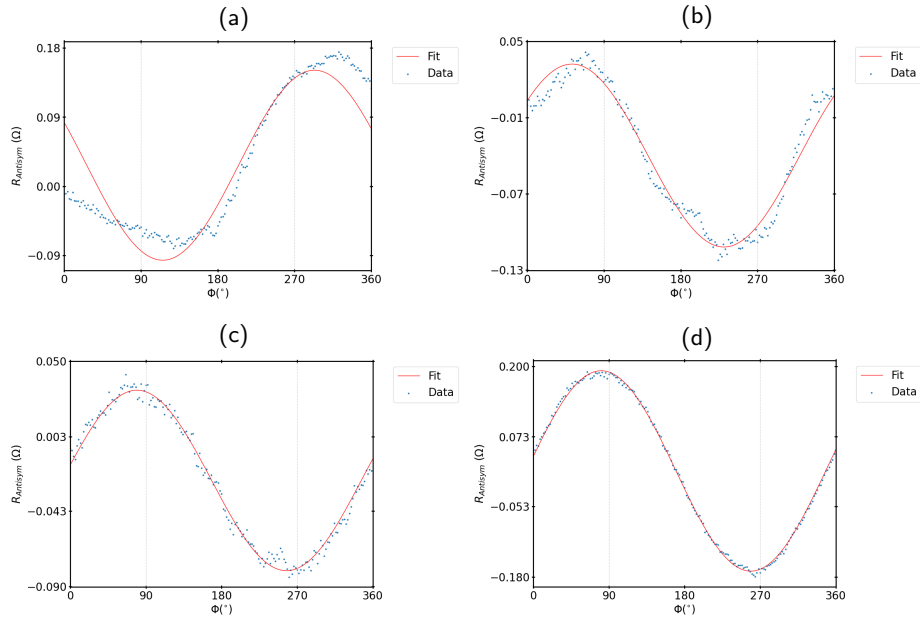


Figure F.2: Antisymmetric part of  $R_{xy}$  as a function of the angle of the in-plane magnetic field for a)  $T=6$  K and  $B=400$  mT, b)  $T=6$  K and  $B=1400$  mT, c)  $T=110$  K and  $B=400$  mT, d)  $T=110$  K and  $B=1400$  mT, with their fits, respectively. c)  $B=1400$  mT, and different values of the temperature ( $T=10$  K,  $T=30$  K,  $T=70$  K)

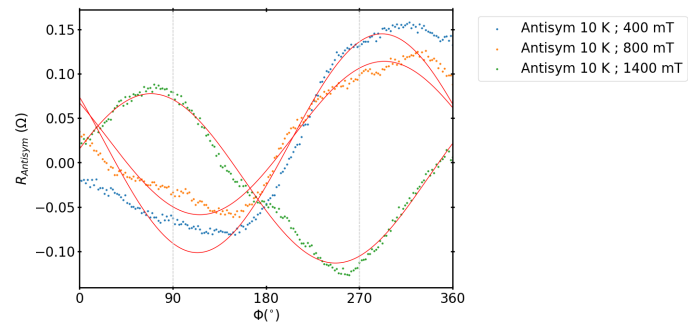


Figure F.3: Antisymmetric part of  $R_{xy}$  as a function of the angle of the in-plane magnetic field for  $T=10$  K, and different values of the Magnetic field ( $B=400$  mT,  $B=800$  mT,  $B=1400$  mT)